Cell Reports
Physical Science

CellPress
OPEN ACCESS

Article

Multi-method characterization of a commercial 1.2 Ah sodium-ion battery cell indicates drop-in potential

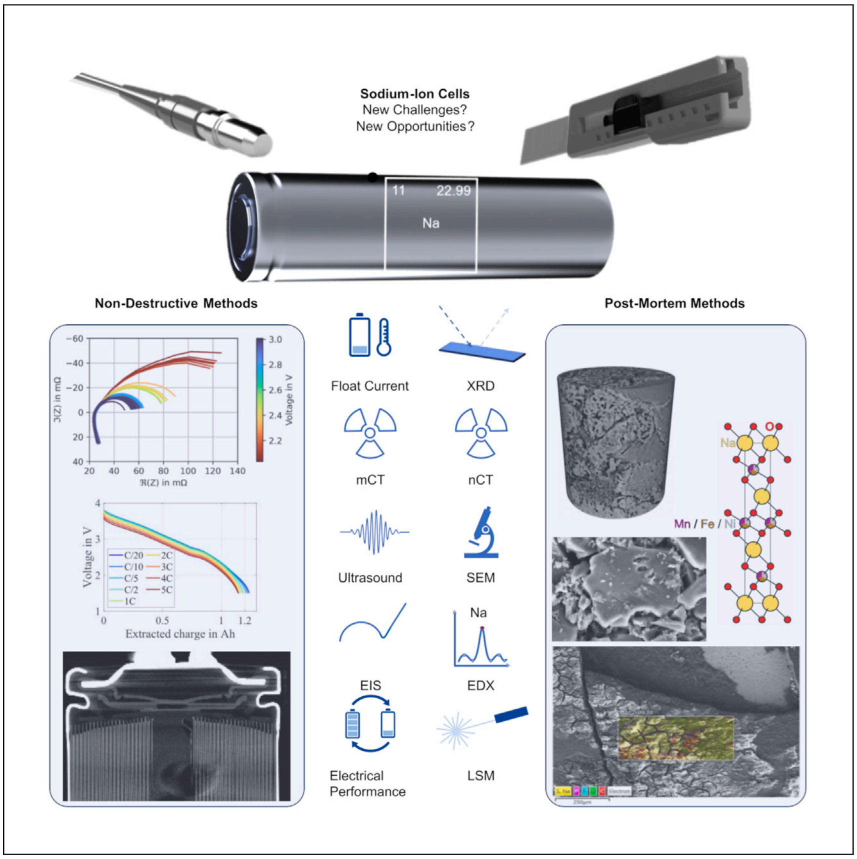

Laufen et al. show that multi-method characterization of a commercial sodium-ion battery benefits from established methods for lithium-ion batteries. They show iron and manganese shares within the cathode and high charging currents have no detrimental effect on capacity retention, indicating this cell is a low-cost solution for high-power applications.

Hendrik Laufen, Sebastian Klick, Heinrich Ditler, ..., Florian Ringbeck, Joachim Mayer, Dirk Uwe Sauer

batteries@isea.rwth-aachen.de

Highlights

High charging currents have no detrimental effect on capacity retention

Early commercial sodium-ion cell is a low-cost solution for high-power applications

Sodium-ion batteries benefit from established methods for lithium-ion batteries

Laufen et al., Cell Reports Physical Science 5, 101945
May 15, 2024
https://doi.org/10.1016/j.xcrp.2024.101945

Cell Reports
Physical Science

CellPress
OPEN ACCESS

Article

Multi-method characterization of a commercial 1.2 Ah sodium-ion battery cell indicates drop-in potential

Hendrik Laufen,[1,2,3,8] Sebastian Klick,[1,2,3,8,9,*] Heinrich Ditler,[1,2,3,8] Katharina Lilith Quade,[1,2,3,8] Adrian Mikitisin,[3,4,8] Alexander Blömeke,[1,2,3,8] Moritz Schütte,[1,3,8] David Wasylowski,[1,2,3,8] Morian Sonnet,[1,2,3,8] Laura Henrich,[3,5,7] Alexander Schwedt,[4] Gereon Stahl,[1,2,3] Florian Ringbeck,[1,2,3] Joachim Mayer,[3,4] and Dirk Uwe Sauer[1,2,3,6]

SUMMARY

This study presents a multi-method characterization of a commercial 1.2 Ah 18650 sodium-ion battery cell. Many characterization methods used for lithium-ion batteries can be applied to sodium-ion-based cells. Analytical methods, such as ICP-OES and EDX measurements, are in good agreement with the XRD experiment and show high shares of Fe and Mn within the Mn/Fe/Ni-based layered oxide cathode. This enables a low-cost sodium-ion battery. Mercury porosimetry reveals high porosities. Electrical characterization highlights the high-power capabilities of this cell as well as an acceptable transferability of diagnostic algorithms. Despite higher charging currents having no detrimental effect on capacity retention, excessive electrolyte decomposition triggers the cell's current interrupt device, preventing a profound lifetime analysis. This early commercial sodium-ion cell is a low-cost solution for high-power applications. Overall, the characterization of a commercial 1.2 Ah 18650 sodium-ion battery cell benefits from the established methods for characterization of lithium-ion battery.

INTRODUCTION

From storing energy from intermittent renewable sources to powering mobile applications, lithium-ion batteries are found in many energy storage applications. However, lithium and other materials used in lithium-ion batteries such as nickel and cobalt are limited.[1] It has been argued that, even when considering battery recycling, there are insufficient resources to meet the demand, especially considering cobalt.[1] Sodium-ion batteries might offer a solution for this issue due to the use of less scarce materials, and the abundance of sodium.[2] Following numerous publications and scientific interest in recent years, the first sodium-ion batteries are now being introduced to the market. Natron energy already offers battery packs for uninterruptable power supply and peak shaving applications based on Prussian blue anode and cathode.[3] Other companies including startups and large battery manufacturers also announced their products to enter the market in the near future or took steps to prepare for wider market penetration.[4–6]

Sodium-ion batteries are a drop-in technology for lithium-ion batteries, requiring similar production processes and machines as their lithium-based counterparts.[7] This also applies to many methods used to analyze and characterize these batteries.[8]

---

[1] Chair for Electrochemical Energy Conversion and Storage Systems, Institute for Power Electronics and Electrical Drives (ISEA), RWTH Aachen University, Campus Boulevard 89, 52074 Aachen, Germany

[2] Juelich Aachen Research Alliance, JARA-Energy, 52425 Jülich, Germany

[3] Center for Ageing, Reliability and Lifetime Prediction of Electrochemical and Power Electronic Systems (CARL), RWTH Aachen University, Campus Boulevard 89, 52074 Aachen, Germany

[4] Central Facility for Electron Microscopy (GFE), RWTH Aachen University, Ahornstrasse 55, 52074 Aachen, Germany

[5] Chair for Ageing Processes and Lifetime Prediction of Batteries, Institute for Power Electronics and Electrical Drives (ISEA), RWTH Aachen University, Campus Boulevard 89, 52074 Aachen, Germany

[6] Helmholtz Institute Münster (HIMS), IEK-12, Forschungszentrum Jülich, 52425 Jülich, Germany

[7] Chair of Solid State and Quantum Chemistry, Institute of Inorganic Chemistry, RWTH Aachen University, Landoltweg 1a, 52074 Aachen, Germany

[8] These authors contributed equally

[9] Lead contact

*Correspondence:
batteries@isea.rwth-aachen.de

https://doi.org/10.1016/j.xcrp.2024.101945

However, to the best of our knowledge, no report on the post mortem analysis, characterization, and cyclic aging of commercially available sodium-ion batteries has been published so far. This hinders the adoption of sodium-ion batteries as many parameters that are crucial for applications such as achievable lifetime, capacity fade trajectories, and the tolerable temperature window are unknown. In this study, we apply various methods used for characterization of lithium-ion batteries to analyze one of the first commercially available sodium-ion batteries. We investigate whether new challenges for characterization and analysis arise compared with commercially available lithium-ion batteries. We also investigate the thermal stability of this cell. Our analysis allows for a systematic comparison between sodium-ion batteries (SIBs) and lithium-ion batteries (LIBs).

RESULTS

Experimental

The first sections focus on destructive postmortem analysis of a 1.2 Ah 18650 cell as described below. An overview of the cell is given based on a teardown and manufacturer information. Subsequently the active material is investigated by half-cell measurements, followed by the characterization of the electrolyte using gas chromatography-mass spectrometry (GC-MS) and inductively coupled plasma-optical emission spectrometry (ICP-OES). The active material is further analyzed by Hg-porosimetry, powder X-ray diffraction (XRD), scanning electron microscopy (SEM), energy-dispersive X-ray spectroscopy (EDX), and ICP-OES. These insights are complemented by electrical characterization with electrochemical impedance spectroscopy (EIS), C-rate, and float current tests. Successive cyclic aging is investigated by non-destructive methods such as micro-CT as well as ultrasonic measurements of the aged cells.

Investigated cell

The cell investigated in this study is a 1.2 Ah 18650 cell made by Shenzhen Mushang Electronics. Based on the cell specification of the manufacturer and postmortem analysis, a broad overview of the cell is given in Table 1.

To compare the cell's specification with existing LIB, the ENPOLITE-plot developed by Dechent et al.[9] is used. It provides a comprehensive classification of service life, considering the cell's performance in terms of energy and power density.[9] In light of the cell's high specific power density (810 $\mathrm{W\,kg^{-1}}$), its moderate specific energy density (97 $\mathrm{Wh\,kg^{-1}}$), and its service life at high C-rates (refer to section cyclic aging), this SIB effectively bridges a gap that other cell types, as stated by ENPOLITE, are unable to fill. Thus, this SIB cell is a promising candidate for high-power applications.

We opened the cell at its discharge voltage of 1.5 V (60 mA constant current [CC]-constant voltage [CV] discharge down to 1.5 V until $I < 1$ mA) under an inert argon atmosphere in a glovebox (glovebox-type MBRAUN LABstar, O_2 concentration < 0.5 ppm, H_2O concentration < 0.5 ppm). Geometric parameters were measured and samples harvested for further analysis, following the established protocols for lithium-ion batteries published elsewhere.[10,11]

The jelly roll (≈26 g, dry) inside the casing (≈7.4 g) consists of one double-coated cathode, a separator, one double-coated anode, and a second separator. The displacement of the cathode, anode, and separator at the outer end of the jelly roll was measured prior to unwinding. Figure S1A schematically depicts the measured displacement. With 704 mm in length the cathode is shorter compared with the 769 mm long anode. The cathode has a width of 57.5 mm and is narrower

Table 1. Cell specification according to the manufacturer and post mortem analysis

Cell specification		
Nominal capacity	1.2 Ah	
Nominal voltage	3.0 V	
Unit price	1.1 USD/pcs (0.31 USD/Wh)	
Cell dimension (∅ × H)	18 × 65 mm	
Approx. weight	37 g ≅ 97.30 Wh kg^{-1}	
Internal resistance	≤25 mΩ (1 kHz at 50% SoC)	
Voltage limits	1.5–3.8 V	
Continuous current limits	charge 0.6 A (0.5C) at 0°C–10°C	
	charge 1.2 A (1C) at 10°C–20°C	
	charge 3.6 A (3C) at 15°C–25°C	
	charge 6.0 A (5C) at 20°C–45°C	
	discharge 9.6 A (8C) at 10°C–50°C	
Post mortem analysis		
		Separator
Material		polymer without coating
Thickness		15 µm
Porosity		40.6% (Hg-intrusion)
		electrolyte
Material		DMC:EMC:EC:PC:EP
Solvent mass		3.4 g
	Positive electrode	Negative electrode
Active material	layered oxide (NaMO$^{2)}$	hard carbon (HC)
Porosity	29.9 % (Hg-intrusion)	31.4% (Hg-intrusion)
Coating weight	31.61 mg cm^{-2}	16.02 mg cm^{-2}
Coating area	798.1 cm^2	857.86 cm^2
Number of sheets	1 (double coated)	1 (double coated)
Dimension (L × W × T)	704 × 57.5 × 0.111 mm (double coated)	769 × 59 × 0.154 mm (double coated)
Thickness of current collector	17 µm (aluminum)	6 µm (copper)

compared with the anode with 59 mm in width. The geometric overhang, based on the difference of the coated areas of anode (857.86 cm^2) and cathode (798.10 cm^2) amounts to 59.76 mm^2 or roughly 7% of anode area. The thicknesses of the anode and cathode, based on SEM cross-sections as shown in Figures S1B and S1C, are 160 and 128 µm, respectively. The anode features a copper current collector (6 µm thick). The aluminum current collector on the cathode has a thickness of 17 µm. Thus, the coating thicknesses of the anode and cathode are 76–78 µm and 55–56 µm, respectively.

After separating the cell components the electrolyte solvent evaporates. This enables an estimation of a lower boundary of expected solvent mass in the cell. The difference of the mass of all components of the cell after separation and drying, and the mass of the full cell, is 3.4 g.

Electrolyte

Electrolyte extraction is a challenge in lithium-ion battery research. Different methods can be found in the literature (e.g., extraction with supercritical CO_2,[12] extraction with a centrifuge[13]). We investigate the use of a centrifuge to extract the electrolyte from sodium-ion batteries for characterization and coin-cell assembly.

First, the cell was discharged to its discharge voltage of 1.5 V (600 mA CC-CV discharge down to 1.5 V until I < 1 mA). Then the cap of the 18650 cell, consisting of the positive terminal as well as the current interrupt device (CID), was removed under an inert argon atmosphere in a glovebox (glovebox-type MBRAUN LABstar, O_2 concentration < 0.5 ppm, H_2O concentration < 0.5 ppm). Afterward, the capless cell was placed in a 3D-printed cell holder (including a 1.5 mL autosampler vial for the extracted electrolyte). This assembly was then inserted to a conical centrifuge tube. The conical centrifuge tube is airtight after closing its screw cap. The used centrifuge is a Sigma 3-18KS. The centrifugation process starts at 4,000 rpm and ends after several stepwise increases to 10,000 rpm. The autosampler vial in the cell holder was changed under argon atmosphere between two rotation steps. The centrifuged electrolyte was then diluted with dichloromethane (1:100) and afterward analyzed using a GC-MS system (Clarus 680, PerkinElmer). Further information about the used GC-MS analysis can be found in Weber et al.[14]

The centrifuge extracted around 3.0 g of colorless electrolyte from one cell after 6 h. This is less than the lower boundary calculated in investigated cell. Thus, not all of the electrolyte is extracted, which is also the case with lithium-ion batteries.[13] The GC-MS enables the identification of components of this sample. Figure S2 shows the chromatogram with the detected organic solvents of the electrolyte: dimethyl carbonate (DMC), ethyl-methyl carbonate (EMC), ethyl propionate (EP), ethylene carbonate (EC), and propylene carbonate (PC). Mixtures of DMC, EMC, PC, and EC are very well investigated for SIBs in the literature.[15–18] On the other hand EP is not as widely used as the other four solvents. Nambu et al.[19] investigated the use of EP and monofluorinated EP as solvents in lithium secondary batteries. Possible advantages are high relative permittivity and low viscosity in comparison with DMC and EMC resulting in the possibility of lower internal resistance. With a similar intention EP was used as an additive with different concentrations in a 1 M $LiPF_6$:EC:DEC electrolyte system in a $LiCoO_2$/graphite full cell by Kufian et al.[20]

Three 200 μL samples of the extracted electrolyte were analyzed via ICP-OES. The process is explained in inductively coupled plasma-optical emission spectrometry. The average measured concentration of Na in the extracted electrolyte is 1.42 mol L^{-1}. The measured concentration of phosphorus is 1.83 mol L^{-1}. This is substantially higher compared with the sodium concentration. This could indicate a phosphorus-containing additive and $NaPF_6$ as conductive salt, or soluble phosphorus species in the electrolyte as by-products of the secondary electron imaging (SEI)-forming reactions.

In conclusion, electrolyte investigation processes developed for LIBs can also be applied to SIBs. We were able to extract sufficient electrolyte for qualitative characterization and coin-cell building. The results of the characterization show a chemically similar composition as in LIBs of cyclic and linear carbonates. Thus, processes developed for electrolyte analysis in LIBs are also applicable for SIBs.

qOCV-fitting

By fitting the potential curves of anode and cathode to the full cell we gain insights into aging modes, such as loss of lithium inventory, or active material degradation, and design choices of the cell manufacturer such as the n/p ratio.[21] Thus, the calculation of this balancing can be a very valuable tool. To test the transferability of this method to SIBs we applied the algorithm described by Li et al.[22] to the investigated SIB. The aim was to determine the balancing of the SIB by reconstructing the full cell open-circuit voltage (OCV) from the half-cell OCVs.

A C/20 (60 mA) quasi OCV (qOCV) of the full cell was used as reference data for the fitting process. The qOCV was measured with a Neware BTS-4000 Series 5V6A battery tester, by applying a CC without any CV phase within the cell's standard operating voltage window, as stated in Table 1.

We used coin cells (type CR2032) with sodium vs. hard carbon or cathode material, respectively, to get qOCVs for both anode and cathode as input for the fitting process. The material was harvested from a disassembled cell, while the sodium chip (15.6 mm) was purchased from AOT Battery. The coating of the harvested material was mechanically removed on one side to avoid any unwanted influence of the backside.[23] A Whatman GF/C separator with a diameter of 17 mm was used. We used 90 μL of electrolyte in all coin cells. This results in a somewhat larger distance between the two electrodes in the coin cell. Assuming similar porosity compared with the polymer separator of the cylindrical cell, we calculated the additional resistance due to the increased thickness to be in the range of a few mΩ.

Regarding the electrolyte, we used the extracted electrolyte but also prepared cells with a mixture of EC and PC (1:1) with 1.2 M $NaPF_6$ (E-Lyte Innovations, Münster, Germany) as this mixture was reported as a good candidate for sodium ion batteries.[15] The coin cells were assembled in an argon-filled glovebox. For further information the process is described in more detail in Ecker et al.[11]

The coin cells underwent five CC cycles (Neware BTS-4008-5V10mA) with a current of C/50 (60 μA) without any rest phases between charge and discharge. The current was calculated based on the nominal capacity of the full cell multiplied by the area ratio of the coin cell with respect to the full cell. This results in an expected coin cell capacity of 3 mAh. The voltage limits for the anode and cathode are set to 1.5–0.01 V and to 3.9–2.2 V, respectively. All coin cells with the extracted electrolyte showed multiple voltage drops during cycling. The voltage and current data for these coin cell cycles can be found in the appendix (cf. Figure S3). A possible reason for these voltage drops could be an unwanted contact with atmosphere during the transport of the extracted electrolyte. Since the coin cells with the extracted electrolyte did not work as expected, the following results are based on the coin cells with 1.2 M $NaPF_6$ in EC and PC (1:1). The capacities measured with these cells were 3.20 and 3.49 mAh for the anode and cathode coin cells, respectively. This is higher compared with the 3 mAh calculated from the full cell. This result is expected as a surplus of sodium allows for the compensation of losses incurred during formation. Furthermore, the voltage window utilized in the full cell might be lower compared with the cycling of the half-cells. Anode coin cells cycled with a current of C/20 (150 μA) only showed a capacity of around 1.8 mAh, indicating large overvoltages (voltage difference between discharge and charge of around 97 mV).

Figure 1 shows the sodification (SO), de-sodification (DSO) qOCV vs. Na/ Na^+, and the differential voltage of the SO/DSO of the anode and cathode. The anode shows a very flat voltage curve from 40% to 100% in comparison with 0%–40% state of charge (SoC). The differential voltage has a characteristic feature at around 10% and 25% SoC. This behavior can be found in the literature for the sodification of hard carbon.[24] The qOCV of the cathode exhibits two regions with different slopes resulting in two plateaus in the differential voltage analysis (DVA).

Due to the large observed overvoltages of the coin cells, the half-cell voltage curves were corrected prior to the fitting process by adding or subtracting half of the voltage difference between charge and discharge at 100% SoC for SO and DSO, respectively. For the hard carbon coin cells this voltage is 22.15 mV and for the layered oxide it is 22.5 mV. This suggests a resistance in the range of over 300 Ω.

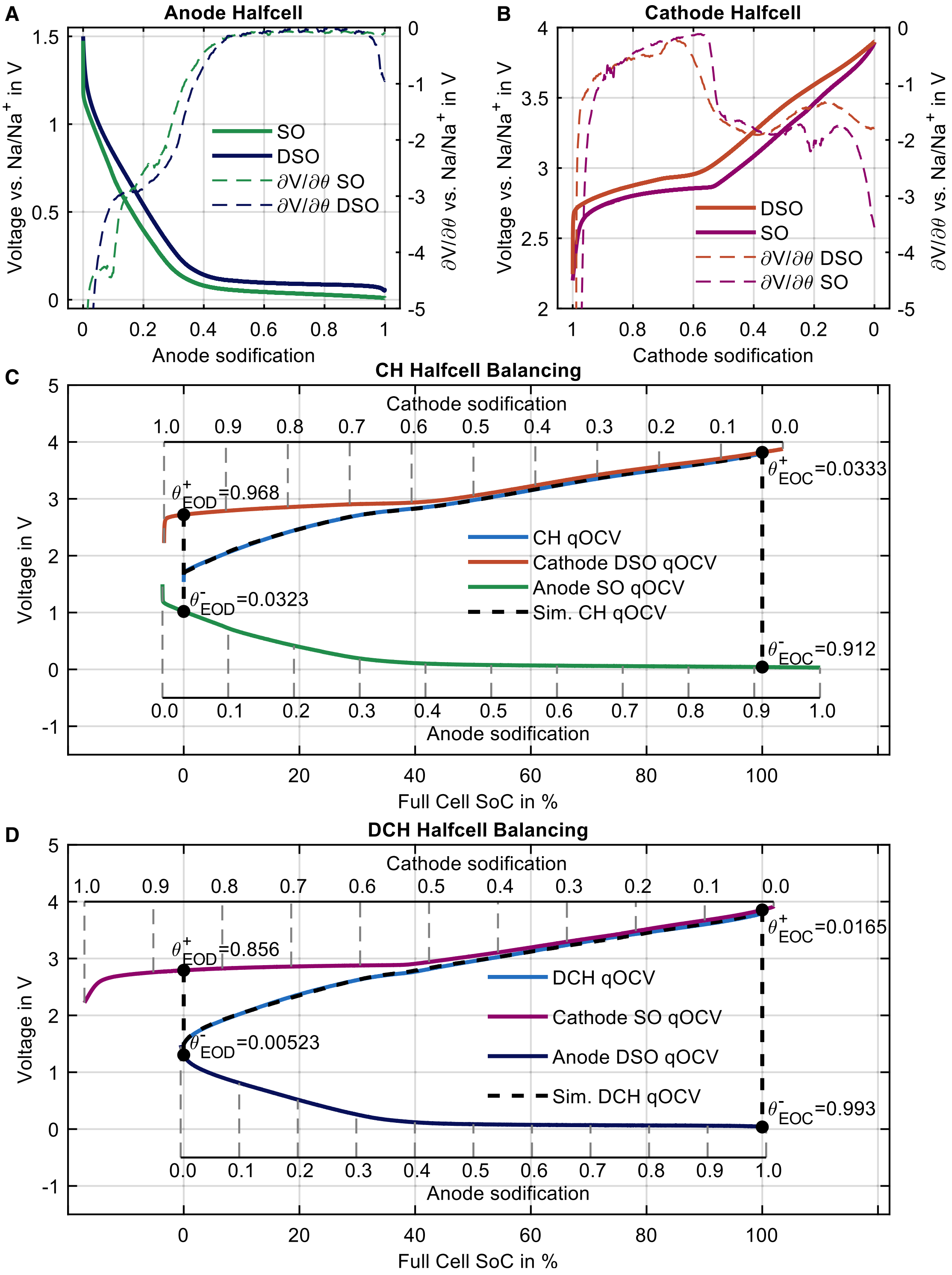

Figure 1. qOCV-fitting of full cell

(A) Anode half cell vs. Na/Na$^+$ SO and DSO qOCV (C/50) and differential voltage.

(B) Cathode half cell vs. Na/Na$^+$ DSO and SO qOCV (C/50) and differential voltage.

(C) Measured full cell CH qOCV (C/20); simulated full cell CH qOCV based on fitted anode SO and cathode DSO qOCV.

(D) Measured full cell DCH qOCV (C/20); simulated full cell DCH qOCV based on fitted anode DSO and cathode SO qOCV. The corrected half-cell voltage curves are only shown in (C and D). Anode and cathode SoC from 0 to 1 is the amount of charge normalized to the capacity during SO and DSO, respectively.

As the different separator only increases the resistance in the range of mΩ, we attribute this resistance to a resistive surface layer on the sodium-metal counter electrode. This is in line with the findings in Bommier et al.,[25] where a strong influence of the sodium counter electrode on the overvoltage was confirmed.

In Figure 1C, the anode SO and cathode DSO qOCVs, the fitted cell balancing charge (CH) qOCV, and the measured CH qOCV of the full cell are shown. The fitting of the half-cell curves is based on the Cuckoo search optimization algorithm, which has been used before for cell balancing.[22,26] The root mean-square voltage error of this fitting is 6.81 mV. Complementary to this, Figure 1D shows the anode DSO and cathode SO qOCVs, the fitted cell balancing discharge (DCH) qOCV, and the measured DCH qOCV of the full cell. Here the root mean-square voltage error is 12.4 mV. The fitted anode and cathode SoC parameters show a significant difference at the low voltage end of the anode and cathode half cells. Due to the flat area of the anode voltage, the fitting of a hard carbon anode in SIBs is more difficult than fitting of a graphite anode in LIBs, which provides multiple features due to phase transitions.[27] For the fit to the charging curve presented in Figure 1D, the results show that, at the lower end of the SOC axis sodium would still remain in the hard carbon anode. Furthermore, even with a fully sodiated cathode some sodium would remain in the anode. This is not supported by the discharging curves, which are limited by the fully desodiated hard carbon anode, as expected. The conflicting results show that further efforts are required to achieve reliable results for the balancing based on half-cell qOCV curves. The results might also be disturbed due to the high overvoltages observed in the half-cells. Thus, reducing this overvoltage by adapting the electrolyte could provide a possible solution.

Porosity

Mercury porosimetry allows to analyze the porous structure of anode, cathode, and separator.[11,28] The low-pressure module Pascal 140 (Thermo Fisher Scientific) was used in combination with the high-pressure module Pascal 440 (Thermo Fisher Scientific) with a maximum pressure of 4,000 bar. The sample size for the double-sided coated anode and cathode was around 44 × 90 mm. The calculation of the results is based on the software SOLID and methods from literature.[10] In Figure 2A, the porosity and the normalized distribution of the pore radii are shown. The pore size distribution of the separator has its maximum at around 87.5 nm. The separator has a porosity of around 40.6%. The anode shows the biggest pore maximum at around 687 nm with a porosity of around 31.4%, similar to the cathode porosity of around 29.9%. The cathode pore distribution has two peaks. The bigger and more frequent pore diameter is at around 468 nm and the smaller one is at around 84.5 nm. The particle size distribution in Figure 2B is calculated similarly to the pore size distribution in Figure 2A, which results in a similar shape. The most frequent particle diameter of the anode is at around 3630 nm. The cathode peaks can be found at around 493 and 2,680 nm.

In comparison, Schmalstieg et al.[10] characterized the porous structures of a high-power $LiNi_{1/3}Mn_{1/3}Co_{1/3}O_2$/graphite cell with the same method. The anode shows nearly the same porosity (31.4%) and around 250% higher particle radius 6,300 nm. The cathode porosity, on the other hand, is 9% lower (20.9%), while the most frequent particle radius is around 60% higher at 2,130 nm. The difference in the separator porosity (40.6%) is negligible.

In Bai et al.,[29] hard carbon for SIBs carbonized at different temperatures was investigated. The best performing variant showed the most frequent particle size at around 8,000 nm. Similar values for the average particle size of multiple hard carbon variants can be found in Yang et al.[30] These sizes are substantially larger than the ones we identified in this cell.

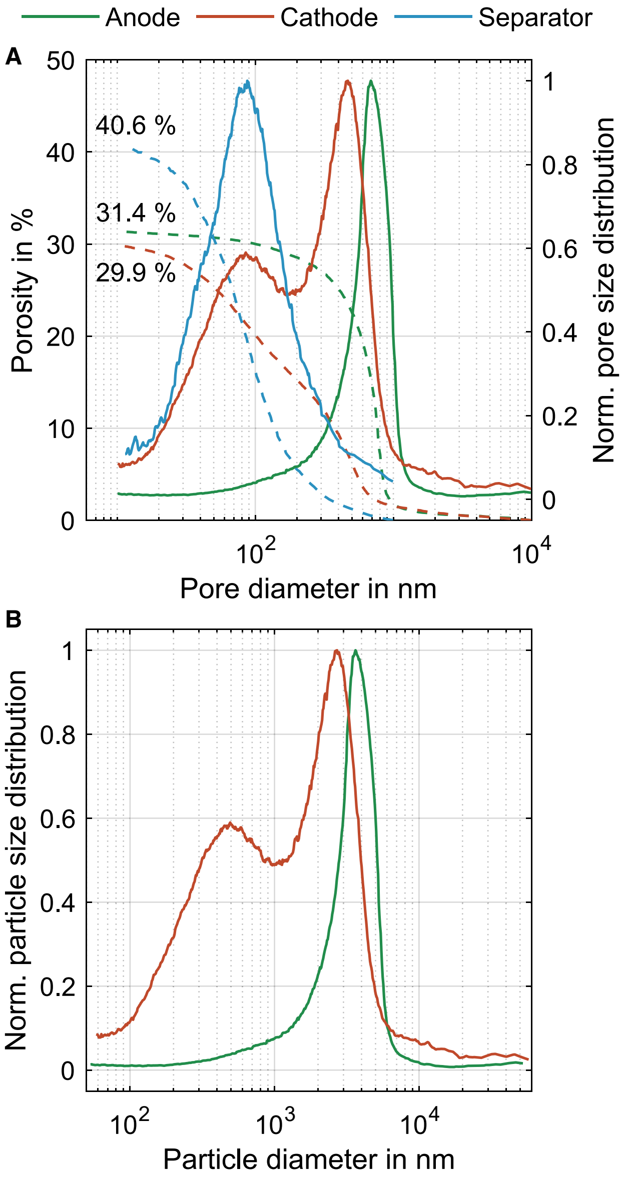

Figure 2. Porosity and particle radii of the electrodes

(A) Porosity (dashed) and the normalized distribution of the pore radii (solid) of the anode, the cathode, and the separator.

(B) Normalized distribution of the particle radii of the anode and the cathode.

ICP-OES

ICP-OES enables the identification of the composition of the anode and cathode. It is widely used in lithium-ion battery research.[10,31,32]

The used ICP-OES measuring device is a Thermo Scientific iCAP PRO. This method is not able to detect the elements C, O, and F. Via ICP-OES the composition of the anode and the cathode was measured. Three double-coated samples of each electrode were punched with a diameter of 20 mm. Without rinsing, samples were dissolved in 12 mL of aqua regia (3 HCl : 1 HNO_3) on a hot plate set to 170°C for about 10–15 min. Afterward the solution was filtered and then diluted to 100 mL with deionized water. The averaged results of each electrode in Table S1 are discussed in the following section ESM and EDX. As the samples presented in Table S1 were not rinsed, conductive salt, which remains on the particle, will result in additional sodium. This is detected in the ICP-OES measurement but is not part of the active material, or any SEI layer.

SEM and EDX

SEM and EDX measurements are widely used in lithium-ion battery research to identify morphology changes, particle cracking, or elemental composition of electrode surfaces.[33–35] Lithium is only measurable with special EDX detectors because of its low X-ray transition energy (Kα at 54.3 eV[36]). Sodium, on the other hand, has an X-ray transition energy of about 1,041 eV[36] and is, therefore, measurable with most standard detectors. This facilitates EDX measurements compared with lithium-ion batteries since sodium-containing deposits can be detected and visualized.

Here, backscattered electron and SEI on the electrode cross-sections were performed in a Zeiss GeminiSEM 300 (Zeiss, Germany). The microscope is equipped with an UltimMax65 EDX detector (Oxford Instruments), which was used for EDX measurements. The accelerating voltage was 15 kV for these measurements.

Figures 3C and 3D show the surface of the anode at two different magnifications, while Figures 3G and 3H present the cathode surface at the same scales.

To complement these measurements, we used a Keyence VK-X1100 confocal laser scanning microscope inside a glovebox. This allows 3D surface imaging of the active materials, as displayed in Figures 3A and 3B and Figures 3E and 3F for the anode and cathode, respectively. The magnification for the laser microscope images is in the same range as the one used for the low-magnification SEM images (Figures 3C and 3G), enabling a direct comparison.

The anode surface reveals single particles, whereas the cathode surface exhibits poly-crystalline structures in both SEM and laser microscope images. The single-particle structure of the anode and poly-crystalline structure of the cathode identified by these imaging methods support the results of porosimetry: one particle size for the anode and two sizes for the cathode. The particle size distribution measured by mercury porosimetry is supported by the high-resolution images (Figures 3D and 3H). The particle sizes measured with the SEM are in the same order of magnitude as the results of porosimetry. Furthermore, the presence of additional components, such as carbon black, is observable in the high-resolution images.

The EDX measurements were conducted on the electrode cross-sections (Figure S1).

The mass fractions for ICP-OES analysis were calculated based on the mass of the coating material. The mass of the coating material is the mass of the punched out electrode without the mass of the current collectors. Since the samples were not rinsed, the mass of coating material and thus the following results contain residual conducting salt.

Sodium, fluorine, phosphorus, and sulfur were detected on both the anode and the cathode using EDX. Furthermore, localized surface depositions consisting of sodium, fluorine, and phosphor were detected in the EDX analysis. This suggests the presence of $NaPF_6$ as conducting salt. Possible sources of sulfur are additives in the electrolyte analogous to LIBs such as 1,3,2-dioxathiolane-2,2-dioxide, propane-1,3-sultone, ethylene sulfite, sulfopropionic acid anhydride, or prop-1-ene-1,3-sultone[37–39] or maybe an electrolyte salt blend with, e.g., NaTFSI.[40,41]

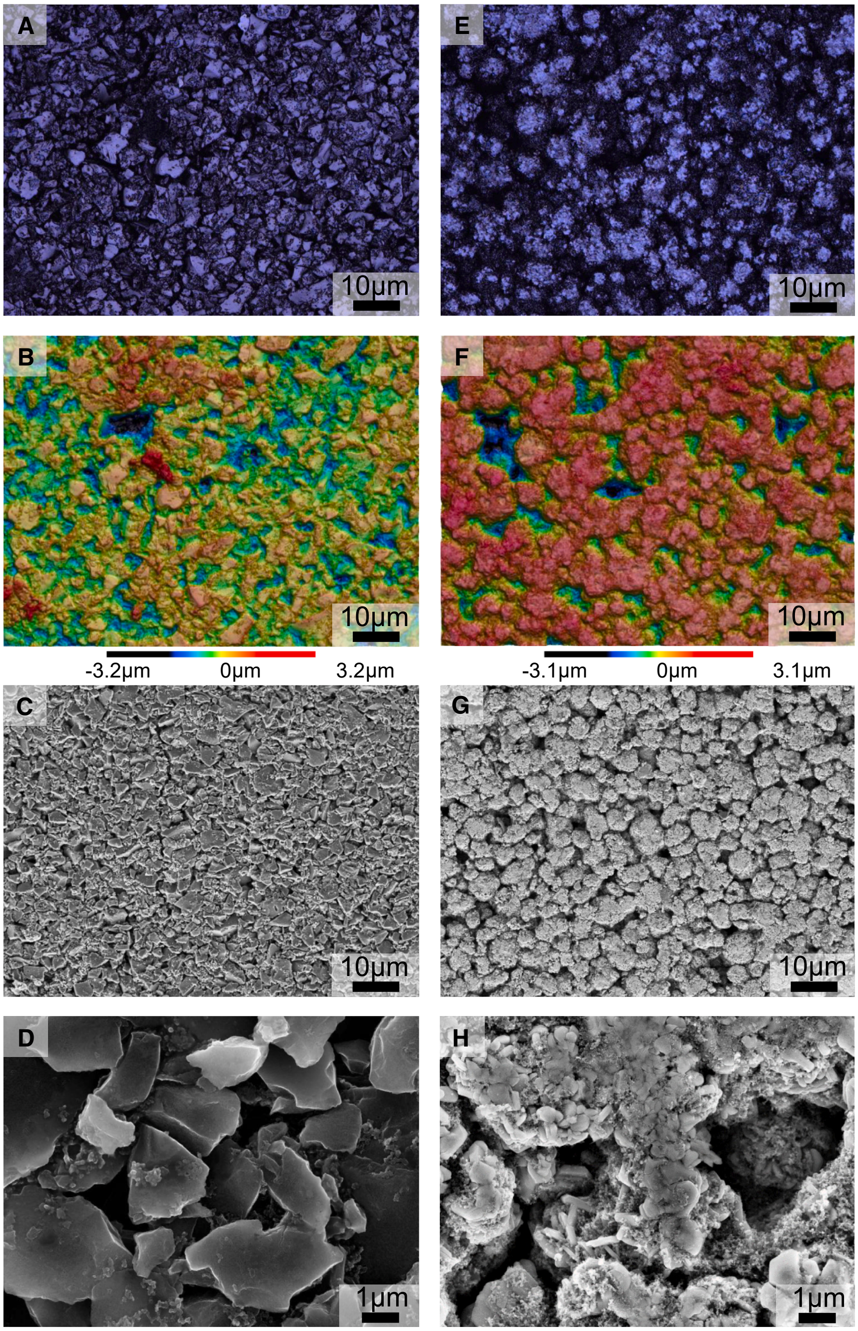

Figure 3. SEM images of the electrodes
Comparison of confocal laser scanning microscopy (anode A and B, cathode E and F) with scanning electron microscopy (anode C and D, cathode G and H). The anode surface reveals single particles, whereas the cathode surface exhibits poly-crystalline structures. Scale bars are 10 μm (A–C and E–G) and 1 μm (D and H).

The elements with the highest proportion based on weight in the cathode are sodium, manganese, iron, nickel (for EDX and ICP-OES measurements), and oxygen (not detectable in ICP-OES). Since manganese, iron, and nickel are present in almost equal proportions for ICP-OES and EDX, a Mn/Fe/Ni 1:1:1 ratio is assumed. After converting the results from weight percent to atomic percent and normalizing the values to the stoichiometry of Na, the cathode structure is $NaMn_XFe_YNi_ZO_2$ with $X = Y = Z$. Normalizing the values to the stochiometry of Na leads to an X of 0.35 and 0.40 for the ICP-OES and EDX, respectively. Since the EDX measurement is focused on an SEM cross-section (shown in Figure S1C), and the samples for the ICP-OES measurements were not rinsed, the difference in X between ICP-OES and EDX can be explained by residual conducting salt within the ICP-OES sample.

Powder XRD

To compare the crystal structure of the cathode material in SIB with those used in commercially available LIBs, the crystal structure was studied by XRD. As the cathode cannot be prepared as a single crystal, XRD was used to determine the crystal structure and occupancy of the examined material.[42] The powder sample was first ground and then filled in a capillary to avoid contact with air during measurement. Then the closed capillary was measured on an STOE Stadi-P with copper radiation ($\lambda = 1.54$ Å) for 8 h at 300 K. The measurement was controlled with the WinXPow software.[43] The yielded diffractogram was analyzed and refined with the FullProf Suite software[44] with the least-squares method. As a profile description, a pseudo-Voigt profile function was used.

EDX and ICP-OES measurements show that sodium, manganese, iron, and nickel are the metals present in the sample. Furthermore, it is expected that the cathode material is a layered structure of alternating metal and oxygen layers, since this structure is necessary to ensure its functionality. There are two possible compounds with different occupations of the manganese/iron/nickel position reported in the literature.[45,46] With both occupancies, a Rietveld refinement was performed, showing that the occupancy from Mao et al.[45] fits better as a starting point. Subsequently, the occupancy of the Mn/Fe/Ni position was changed to a ratio of 1:1:1, so 33.3%, respectively, because the ICP-OES analysis shows that the transition metals should occur in equal proportions of about 1/3. The refinement is shown in Figure 4, and the corresponding data of the refinement can be found in Table S2.

The structure crystallizes in the trigonal space group $R/3\,mH$ (no. 166) with the lattice parameters $a = b = 2.9639(9)$ Å, $c = 16.1093(8)$ Å, $V = 122.55(8)$ Å, and $Z = 3$. Here, in the direction of the c axis, layers occur in A, B, A, C order, where $A =$ oxygen, $B =$ Mn/Fe/Ni, and $C =$ Na. The refinement of the occupancy of the Mn/Fe/Ni position was not possible, while the refinement of the sodium position shows a full occupation. Although the fitting of the structure model fits quite well with the measured data, not all intensities could be perfectly adjusted. A temperature dependency and preferred orientation can be excluded. Nevertheless, the matching reflection positions show that the correct space group and the matching lattice parameters were found with high certainty. To refine the occupancy of the atom position reasonably, single-crystal XRD has to be carried out. At angles, $2\theta = 24^\circ$ and 43°, two small reflexes can be found. These cannot be assigned to any known substance in the literature. There are two possibilities where these reflexes originate: on the one hand, additional reflections can be caused by symmetry descent due to, e.g., vacancies, or on the other hand, there could be another unknown crystalline substance in the sample. Both must be checked in the future by further analysis, for example, IR spectroscopy. XRD confirmed that the cathode consists of a layered oxide material, which has mixed occupancy at the transition metal position, similar to transition metal oxides in LIBs such as nickel-manganic-cobalt (NMC).[47]

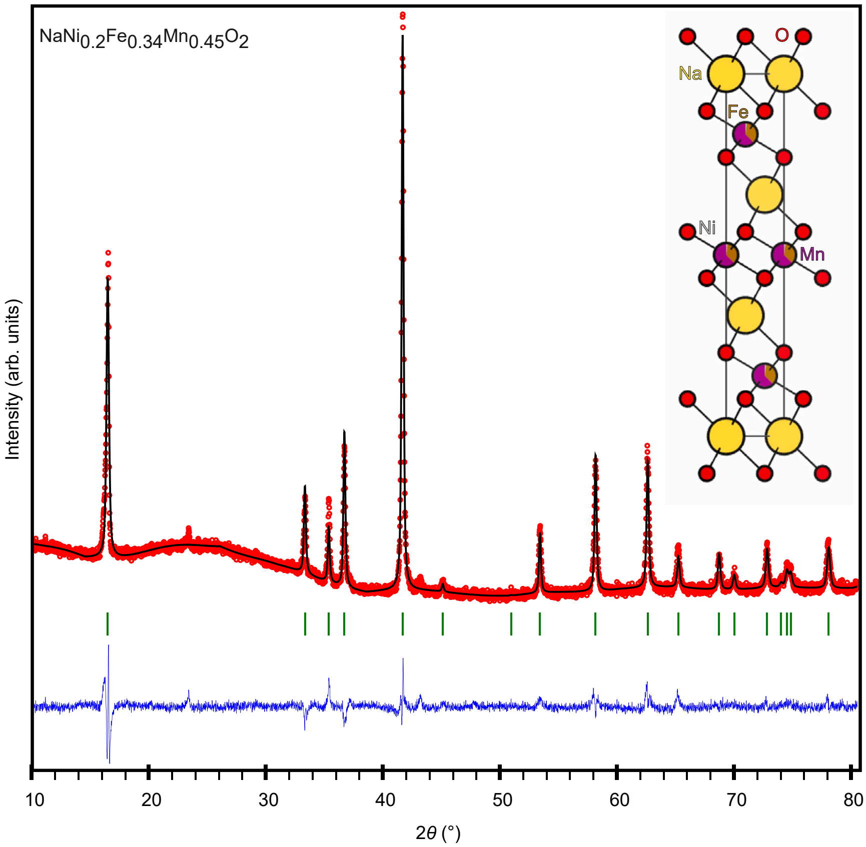

Figure 4. Cathode's Rietveld refinement
Rietveld refinement of the measured cathode material with measured data in red, fitted pattern in black, Bragg positions in green, and difference curve in blue.

Electrical characterization

Accurately characterizing the electrical properties is crucial for evaluating the energy and performance capabilities of lithium-ion cells.[48] Furthermore, conducting a thorough analysis of electrical properties, such as open-circuit voltage and power characteristics, is essential for developing diagnostic algorithms that enable effective monitoring and assessment of cell health and functionality. It also aids in parameter identification of equivalent circuit models.[48,49] In this section, we analyze the voltage and extractable capacity under various current rates with the aim of examining challenges associated with transferring diagnostic methods from LIBs to SIBs. Additional electrical characterizations, such as EIS and float current measurements, are discussed in the following sections.

We conducted a comprehensive characterization of three sodium-ion cells in a controlled climate chamber at an ambient temperature of 25°C using a battery tester, allowing us to obtain an initial assessment of the cell's electrical behavior. First, we carried out a series of capacity tests at various C-rates, ranging from C/20 to 5C. We charged the cells according to the CC-CV charge protocol in the voltage window 1.5–3.8 V, where the criterion for terminating the CV charge was a current below 24 mA of the nominal capacity or a timeout of 60 min. The discharge process was terminated when the discharge cutoff voltage was reached. We repeated the discharge and charge process for every current rate with a 60 min break between charge and discharge, thereby minimizing the impact of current history. Following the tests, we performed a

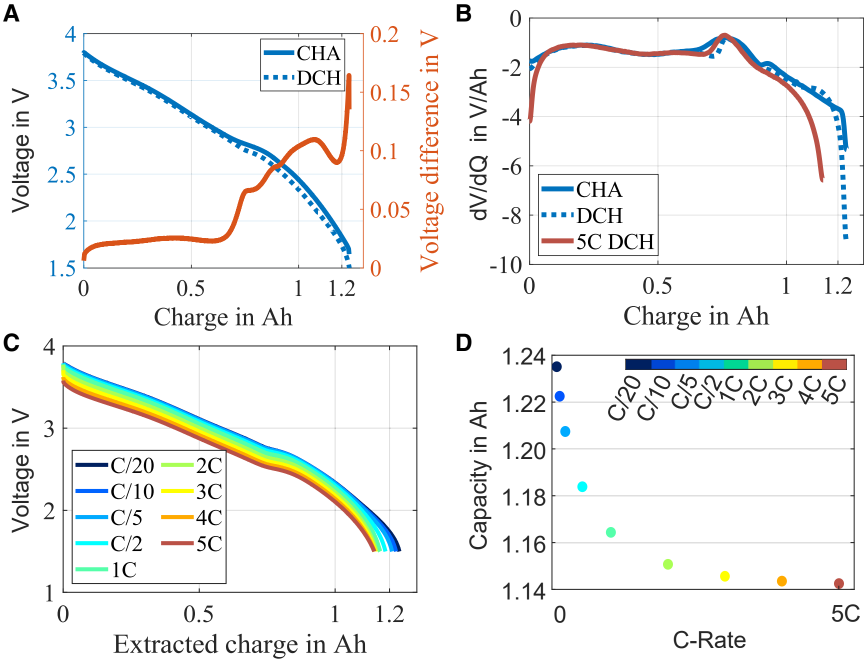

Figure 5. Electrical properties of one cell at an environmental temperature of 25°C

(A) Quasi open-circuit charge and discharge curve. Hysteresis of the cell as the difference between the charge and discharge qOCV curves.

(B) Differential voltage analysis (DVA) for discharge and charge processes as well as for a 5C discharge.

(C) Discharge voltage curves for varying current rates.

(D) Capacity determination for varying current rates.

qOCV measurement at C/20 in the voltage window of 1.5–3.8 V, utilizing the CC-CV method during both the charge and discharge processes. The measurement results are presented in Figure 5. Figure 5A illustrates the qOCV curve of a single cell during both the charging and discharging processes. The curve exhibits a voltage plateau at approximately 0.7 Ah, while the rest of the curve displays a steep slope. The steepness of the qOCV curve enables the application of conventional diagnostic methods that rely on mapping the OCV to the SoC, an essential advantage over LFP/C cells, which show a flat OCV with comparably large hysteresis.[50] The hysteresis of the sodium-ion cell is illustrated in red as the disparity between the charge and discharge voltage curves.[50] It can be observed that, up to 0.6 Ah of extracted charge, the hysteresis is relatively small and constant. However, in the lower voltage range, the hysteresis becomes more pronounced. Figure 5B presents the DVA for the qOCV during both discharge and charge processes, as well as during a 5C discharge. For the analysis of the differential voltage, we used a smoothing spline in the MATLAB environment (i.e., spaps). Notably, due to the utilization of hard carbon anodes in this SIB, the DVA exhibits less significant variations compared with established LIBs.[51] Interestingly, during charge and discharge, the DVA shows minimal differences in the 0–0.7 Ah range. Furthermore, even during a 5C discharge, the measured voltage curve maintains a similar slope compared with the low-current qOCV, offering advantages for diagnostic algorithm application. This characteristic allows the determination of the SoC based on the voltage curve, even without fully relaxing the cell, as the slope for lower charge remains unchanged even at higher currents. Figure 5C depicts the voltage curves during constant current discharge at various C-rates, ranging from C/20 (60 mA) to 5C (6 A). Lastly, Figure 5D shows the corresponding capacities for the different C-rates. At an ambient temperature of 25°C and a constant current discharge rate of 5C, our tests show that we can extract approximately

98.12% of the 1C constant current discharge capacity. This achievement is comparable with other high-power cells such as the LMO/LTO cells tested by Nemeth et al.,[52] where 98.93% of the 1C capacity can be extracted at 5C. Furthermore, our results compare favorably with the high-power NMC/LTO cells examined by Bank et al.,[53] which exhibit 94.89% of the 1C capacity extractable at 5C under the same ambient temperature conditions. Upon initial electrical examination of three sodium-ion cells, it is evident that the steep OCV(SoC) curve provides favorable conditions for the transfer of diagnostic algorithms from established materials to this sodium-ion cell type. However, the presence of hysteresis in the low SoC range will present a challenge when estimating the remaining energy.[54] Our results show that the sodium-ion cells' robust current capability makes the cells well suited for high-power applications since the current capability is comparable with those of established high-power lithium-ion battery cells.

Electrochmical impedance spectroscopy

Changes of LIBs, e.g., in SoC, state of health (SoH), or temperature correlate with their impedance,[55] which can be measured using EIS.

Here, we performed two different sets of measurements on SIBs: initial multisine-EIS measurements of 211 cells (which can be used for quality control), and impedance spectra of 3 cells over 21 equidistant SoCs referred to as characterization impedance spectra in this section. Further measurements of weight, voltage, and 1 kHz impedance of 211 cells complement these results.

Initial multisine-EIS was measured using an ExaMight (Safion GmbH) between 1 and 10,000 Hz. The cells were kept at 21°C for 24 h prior to the measurements and measured as delivered without any prior charge or discharge. The standard deviation of the temperature during the measurements was 0.16 K. The characterization spectra were recorded at 21 equidistant SoCs, starting with the highest SoC after a constant current followed by constant voltage (CCCV) charge with 0.5 An until 3.8 V and a cut-off current of the CV phase of 24 mA at 25°C.

Analyzing the complementary measurements, the weight, and the 1 kHz impedance did not show a significant difference. However, the initial voltage of the cells at delivery differed. Initial multisine-EIS, reveals a correlation between these impedance spectra and the initial voltage, shown in Figure 6A. On closer inspection, there is still a minor difference between impedance spectra for the same initial voltages. Aging tests to be performed will show whether the additional difference in the impedance measurement correlates with the aging behavior.

The galvanostatic characterization impedance spectra were recorded for three cells at 21 equidistant SoCs for the range of 10 mHz to 6 kHz. Each logarithmic decade encompassed eight measured frequencies, with each frequency undergoing a set of three measurements. The current amplitude was controlled to achieve a voltage response of 10 mV while staying below 2 A.

Figure 6B presents the resulting Nyquist diagrams. In the lower SoCs, the impedance increases significantly. With higher SoCs, the impedance change over the SoC decreases. This change of the impedance over SoC is similar to an 18650 LIB battery with an NMC cathode as analyzed in Shafiei Sabet et al.[56]

The EIS measurements indicate that EIS is also applicable to SIBs. Moreover, the measurement results are similar to LIB results. Thus, similar elements can be used for equivalent circuit models of SIB.

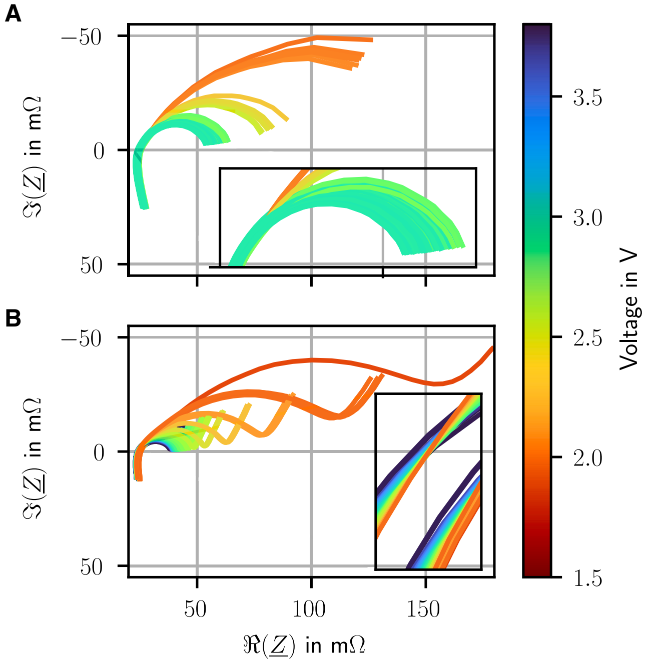

Figure 6. Electrochemical impedance spectroscopy of sodium-ion batteries

(A) Quality assurance measurement of 211 cells.

(B) Initial characterization of 3 cells at ≈25°C measured after a CCCV charge at 21 equidistant SoCs starting with the highest SoC. The enlarged view has a width of 1.5 mΩ.

Float current measurements

The float current is defined as the steady-state current required to maintain the cell under potentiostatic conditions after an initial transient process, also known as self-discharge current.[57] Although the float current can generally be divided into a reversible and an irreversible (capacity loss) component,[58] in the case of nickel-cobalt-aluminum/graphite LIBs, the latter dominates, enabling fast prediction of calendaric aging and extraction of activation energies using the Arrhenius law.[57] This section extends the methodology to SIBs.

In this investigation, four pristine cells were exposed to controlled temperature variations using a laboratory heating oven. The temperature was incrementally raised from 25°C to 55°C in steps of 10 K, and each temperature was maintained for a duration of 48 h. To measure the float current, custom hardware (details of which will be provided in forthcoming publications) was utilized. The float current was measured at the cells' as-delivered voltages, specifically 3.007, 3.014, 3.005, and 2.451 V, respectively. It should be noted that the precise voltage values were not provided explicitly, but rather extracted directly from the connected cell itself. The cell floated at 2.451 V has already lost more than 0.5 V relative to the other cells, indicating a relatively high self-discharge current, presumably due to an internal defect.

Raw measurement data for the first cell are depicted in Figure 7, while the complete set of raw measurement data for all cells can be found in Figure S4. It should be noted that the raw measurement data are significantly affected by noise interference. Therefore, for the subsequent Arrhenius analysis, only the averaged steady-state float current values were taken into consideration. Regarding the averaging process, float current spikes reaching up to 3 mA, which occurred at

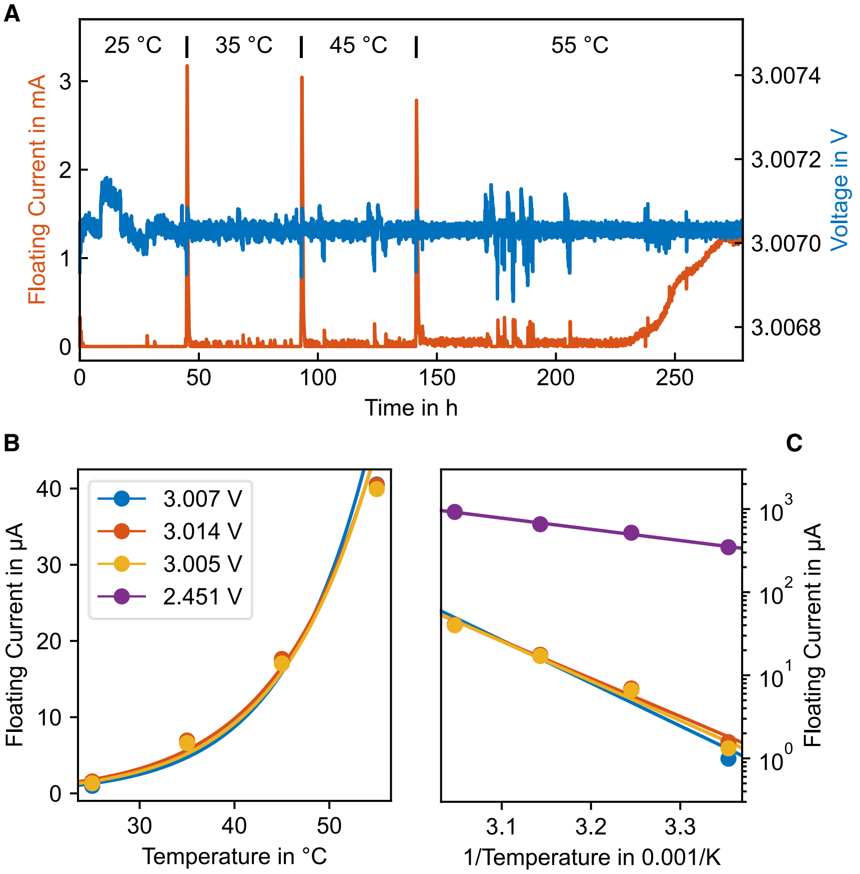

Figure 7. Results of float current measurement

(A) Temporal plot of float current, voltage, and oven temperature for the cell maintained at 3.007 V. The voltage fluctuations observed during the first approximately 48 h at 25°C are attributed to temperature changes in the custom measuring hardware.

(B) Measured (dots) and fitted (solid line) float current for the cells maintained at 3.007, 3.014, and 3.005 V with respect to the oven temperature, displayed on linear axes.

(C) Measured and fitted float current for all cells plotted in an Arrhenius plot. Legend for (B) and (C) is shown in (B). Data points for the first three cells overlap strongly.

each temperature step, were assumed to have decayed within 3–5 h. In addition, the gradual increase in float current, observed after approximately 230 h of operation, was disregarded. This increase was observed in both the first and third cells. Even after cooling the cells to room temperature, the float current remained at approximately 400 µA, giving an approximately 400-fold increase relative to its initial float current. The average steady-state float current exhibited an increasing trend with rising temperature, with values ranging from approximately 1 to 40 µA for the first three cells and from 350 to 924 µA for the fourth cell, as illustrated in Figures 8B and 8C. The voltage fluctuations, observed within the initial 48 h of measurement, can be attributed to a measurement artifact resulting from a shift in the ambient temperature of the measuring circuitry.

The positive spikes in the float current can be attributed to the decrease in the cell's OCV with increasing temperature. According to the Gibbs-Helmholtz relationship, this decrease in OCV signifies a negative change in entropy during the spontaneous discharge reaction of the cell.

The averaged float current can be reasonably well fitted by an Arrhenius relationship, as illustrated in Figure 8C. Consequently, for the first three cells operating at approximately 3.01 V, the activation energy associated with the chemical process leading to the cell's self-discharge can be estimated as 92 ± 5 kJ mol^{-1}. Conversely, for the fourth cell operating at 2.451 V, the activation energy is determined to be 26 kJ mol^{-1}.

The gradual and partially irreversible increase in float current observed in the first and third cells after approximately 90 h at 55°C suggests a spontaneous and irreversible degradation of the cells. According to the datasheet of the cell, the maximum allowable operating temperature for discharge is 55°C. Our findings indicate that the observed spontaneous temperature-induced degradation limits the lifetime of the cell at high temperatures. Further investigation is required to fully comprehend the precise mechanism underlying this degradation process.

The results shown here demonstrate the applicability of float current analysis on SIBs similar to LIBs. The measurement of the float current at varying temperature allows the estimation of the activation energy of the internal self-discharge process and inter-cell comparison of float currents allows for identification of defect cells.

Cyclic aging

In addition to the initial non-destructive and destructive characterization methods the cyclic performance of the cylindrical 18650 SIB cell is of great interest. To obtain a first impression and to explore the performance at its limits, three different combinations of C-rates were applied at room temperature of ≈21°C. For the first test 1C CCCV CH/1C CC DCH cycles (blue, 1C1C) were conducted. For the second one, 3C CCCV CH/8C CC DCH cycles (orange, 3C8C), and for the third test 5C CCCV CH/8C CC DCH cycles (red, 5C8C) were conducted. The detailed test procedure is given in the supplemental information as a flow chart (see Figure S5). Each test procedure was applied to three cells using a Neware BTS-4000 Series 5V6A (for 1C1C) and 5V12A (for 3C8C and 5C8C) battery testers. The discharge capacity of the periodically repeated C/2 discharge capacity test is depicted in Figure 8A. As shown in Figure 8, the capacity increases for all three test procedures until 400 full equivalent cycles (FECs). For 1C1C the C/2 capacity continues to increase. After reaching 600 FECs the discharge capacity (3C8C, 5C8C) starts decreasing linearly. This is confirmed by the C/20 discharge capacity test, as shown in Figure 8B. The C/20 discharge capacity of the 1C1C cycling test continues to increase, supporting the measurement of the C/2 discharge capacity. Comparing the moderate C-rate of 1C1C with aging data of LIBs, this SIB has a very similar cyclic lifetime as cells with LTO anodes[59] or LFP cathodes.[60] Similar to the LTO-LIB tested in Chahbaz et al.,[59] this SIB exhibits a capacity loss of less than 5% after 1,000 FECs with 100% depth of discharge (DOD). In contrast, this kind of SIB exceeds the cyclic lifetime of common NMC/graphite LIB.[61] Exceptionally, special designed cells, for example with single-crystal NMC as cathode material,[61,62] outperform the SIB. As this SIB is considered a high-power cell, the cell is well comparable with the cyclic lifetime of LTO at high C-rates.[59] Similar to the aging data of the SIB in this work, the cyclic aging data of Chahbaz et al.[59] show the same behavior for moderate and high C-rates at 100% DOD until 1,000 FECs. After 1,000 FECs the aging behavior of moderate and high C-rates for both LTO[59] and the SIB splits up.

During cycling, the cells in the test procedures 3C8C and 5C8C reach maximum temperatures of 47°C–52°C and 55°C–60°C, respectively. The temperatures were measured using a thermal camera (FLIR E-Series). In this context, it is worth mentioning that all three cells of the 5C8C test procedure suddenly dropped to 0 V after reaching 1,196, 1,255, and 1,273 FECs, respectively. At this state the cells

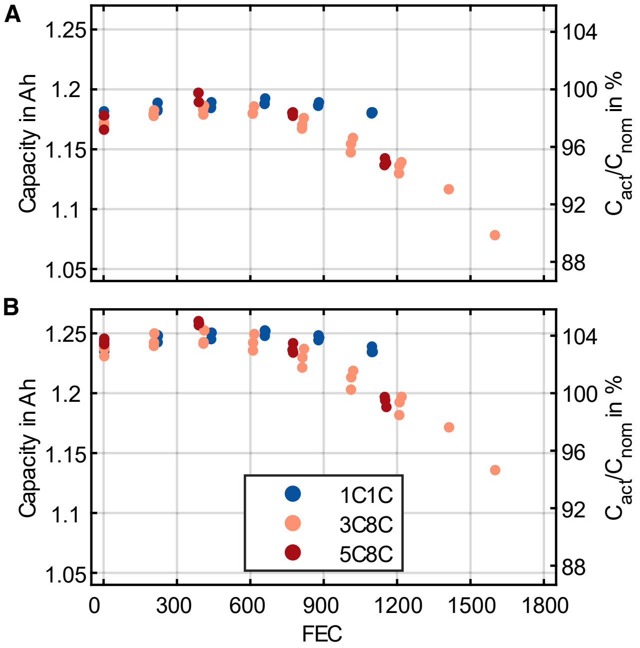

Figure 8. Discharge capacities for different C-rates plotted over FEC

For each cyclic test (1C CCCV CH/1C CC DCH [blue], 3C CCCV CH/8C CC DCH [orange], and 5C CCCV CH/8C CC DCH [red]) three cells were tested at room temperature

Following discharge capacities are shown: (A) C/2 discharge capacity, (B) C/20 discharge capacity.

have lost less than 5% of their initial capacity. Computed tomography (CT) images of the cell show that the CID was triggered (see Figure S6).

Until the sudden cell failure, the capacity decay of cells cycles with both 3C8C and 5C8C behave almost identically. Hence, the substantially higher charging current in the case of the 5C8C protocol does not have a detrimental effect on capacity retention. This underlines the high-power capabilities of this cell. The earlier failure of the cells cycled with 5C8C can be attributed to a higher gas generation, possibly by thermal electrolyte decomposition. This highlights the challenge to overcome the excessive electrolyte decomposition in commercial SIBs.

In principle, the cyclic aging tests are an inevitable method to determine the cyclic lifetime. However, the activation of the CID and the low loss of capacity to this state prevents a profound lifetime analysis.

X-ray microscopy

X-ray microscopy (XRM) is a powerful tool for assisting battery aging tests and evaluation due to its non-destructive nature.[63] It enables a view inside the cell without the need to open it. By rotating the sample by 180°–360° a full set of angular pictures is taken. Using an FDK reconstruction algorithm allows for 3D reconstruction of the investigated sample.[64] After achieving the 3D reconstruction, visual slices can be taken at any point to picture defects within particles of how secondary particles are agglomerated. Thus, structural changes on the macro level can be detected while keeping the cells operational.[65] In contrast to XRM on the micro- and macro-scale, laboratory nano-computed tomography (nCT) requires direct access to the active material. Hence, it is a semi-destructive method, yet it also yields valuable insights into the aging mechanisms of active material on a particle-scale level.[66] Being such a powerful tool, we applied XRM on different scales to the SIB.

A Zeiss Xradia 620 Versa was used for micro-computed tomography (mCT) measurements. An X-ray energy of 160 kV and a current of 156 μA was used to analyze the cell. Figure S6 shows changes of the cell after aging at high current rates (5C8C, as described above). As seen in the right image of Figure S6, the CID has popped, most likely due to gas development inside the cell. In addition, the image shows that the cell has expanded upward despite the steel casing and has even significantly bulged the casing wall due to pressure increase inside the cell. Moreover, the examination of the unaged cell in mCT revealed that the general production quality of this cell was not good. Asymmetrical anode overhangs, as well as bent ends of the anode layers, can already be observed in the unaged cell. In addition, the cell exhibited unevenly large cross-sections.

After opening a fresh cell in a glovebox, the extracted electrode foils were examined using mCT under atmospheric conditions without any further preparation. Figure S7 displays the results of the mCT examination of the anode and cathode. Both foils were measured at 70 kV (10 W) with a pixel size of 500 nm. In this way, mCT enables the estimation of electrode layer thicknesses, as well as particle sizes, distributions, and porosity to be made without any further manual effort and within an acceptable measurement time. The determination of layer thicknesses showed good agreement with previous investigations in SEM and using micrometer screws. The defects within the anode material seen in the CT images are likely due to the manual preparation during cell opening and do not show any production defects.

nCT imaging was conducted using a Zeiss Xradia 810 Ultra nanotomograph. A quasi-monochromatic photon energy of 5.4 keV was used to study the electrodes at the particle size level, with a resolution down to 50 nm. The sample preparation for the nCT was carried out using focused ion beam (FIB) technology, as an approximate sample volume of 15 μm in diameter is optimal for this resolution. While mCT is used to examine statistical quantities such as particle size, particle size distribution, porosity, and major defects, nCT is utilized to investigate features at the particle scale.[66] This includes defects within the particles, the morphology of porosity, and the binder distribution between particles. A correlative workflow between X-ray microscopy and electron microscopy allows for the examination of battery cell aging behavior across the entire length scale, from macro to nano. Figure 9 shows the results of the nCT examination of the anode and cathode. Initially, in the top left image, the sample preparation using a gallium-FIB is depicted. Sample cylinders are prepared from the sample surface using the FIB. Subsequently, the freed volumes are removed from the surface using a micromanipulator and applied to the sample holder of the nCT (tungsten needle), as shown in the middle SEM image and as a projection image within the nCT. The sample volumes prepared in this manner were then analyzed using phase contrast nanotomography. The phase contrast in the Zeiss Xradia 810 Ultra allows for the examination of particle and pore volumes,[67] as well as the high-resolution investigation of binder structures between the particles. Figure 9 presents the results of nanotomography for both the cathode and anode. For the cathode material, both secondary and primary particles can be identified. Furthermore, defects within the primary particles after aging, as well as the structures of the secondary particles, can be resolved. The examination of the morphology of the hard carbon used in the anode reveals a variety of particle shapes and, in some cases, an inhomogeneous distribution of the binder material. Transferring these high-resolution results to the findings of the microtomography enables a cross-scale characterization of aging effects in sodium-ion battery cells.

The application of X-ray microscopy, particularly mCT, and nCT, proved to be an extremely valuable non-destructive tool for investigating and characterizing aging

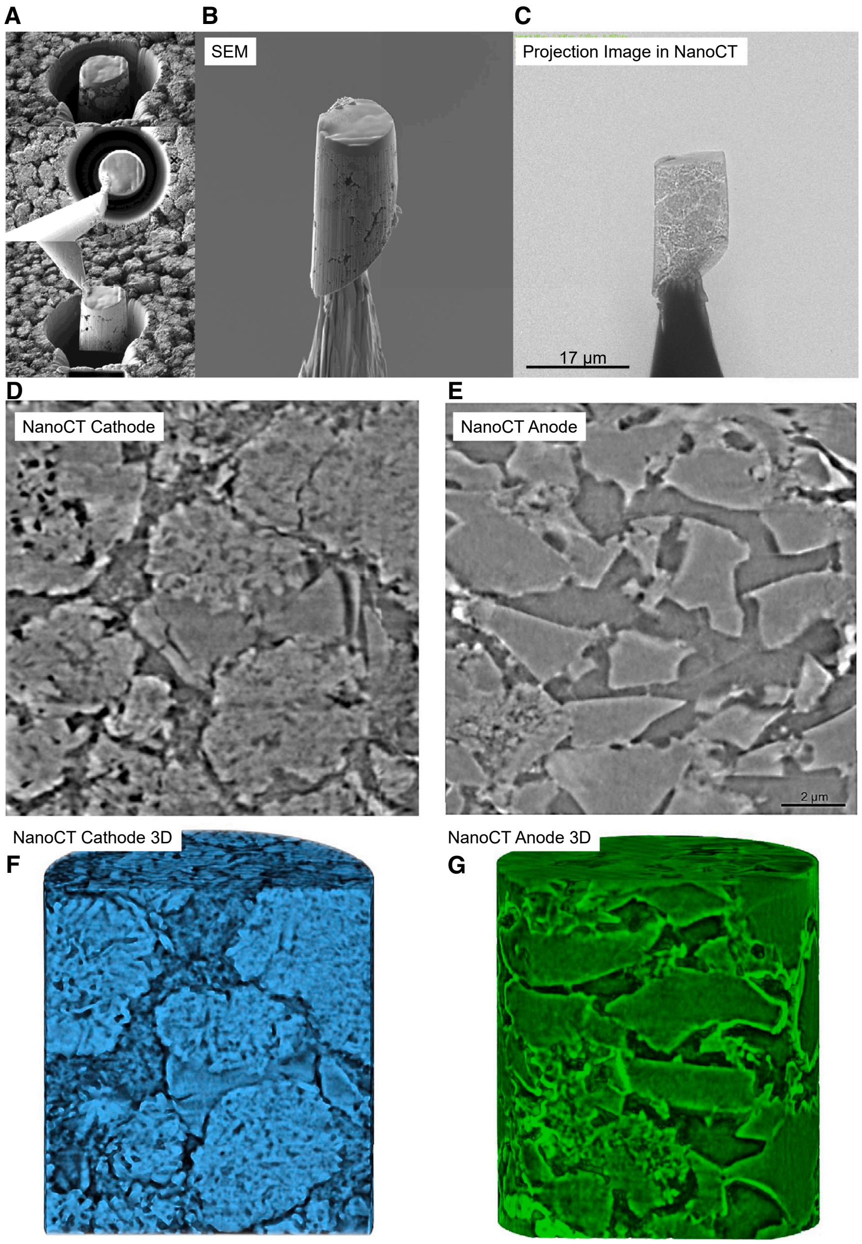

Figure 9. nCT analysis results for the Na-ion anode and cathode

Top left images (A) illustrate sample preparation via FIB; sample cylinders are created using gallium ions and mounted on nCT's tungsten needle with a micromanipulator (seen in middle SEM (B) and projection image (C)). These samples underwent phase contrast nanotomography analysis using a ZEISS Xradia 810 Ultra, enabling inspection of particle/pore volumes and high-res binder structures. The cathode analysis in (D) and (F) reveals the representation of secondary and primary particles, defects in primary particles post-aging, and secondary particle structures. The anode analysis in (E) and (G) shows diverse particle shapes and occasional uneven binder distribution. Scale bars are 17 µm (C) and 2 µm (D and E).

effects in sodium-ion batteries. The technique enabled the collection of detailed data across various scales, from the full cell down to particle properties at the nanometer level. This comprehensive analysis provides critical insights into mechanical deformations, changes in layer thickness, and particle structures within the cells, thereby contributing to the development of more durable and efficient battery systems.

Ultrasound

The role of ultrasonic investigations in LIB cell characterization and diagnosis has been intensively explored in recent years.[68–70] In particular, structural changes within the cell can be detected due to the interaction of the ultrasonic wave with the cell components. Among others, aging effects, gassing, and electrolyte distribution can be measured.[71] The aim of this section is to demonstrate the transferability of the measurement method to SIB cells. Ultrasonic measurement devices usually consist of one or more piezoceramics, which generate a mechanical wave when excited with an electric pulse. While traveling through the active material, the wave is attenuated. Furthermore, transmissions and reflections occur when the acoustic properties of the materials change, for example, at the interface of different materials in the cell. Transmission and reflection depend on the so-called acoustic impedances. To measure the transmitted wave at the opposite end of the battery cell a second piezoceramic is required to convert the mechanical wave into an electrical voltage (see Figure S8A). We investigate whether the materials used in SIBs have similar properties as those in LIBs regarding ultrasound waves. Furthermore, we use ultrasonic measurements to analyze changes in aged SIB.

Analogous to Wasylowski et al.[71,72] we recorded and compared ultrasound measurements of a pristine cell and a cell with triggered CID. For this purpose, we selected the cell that was aged with 5C8C. The ultrasonic sensors were attached to the outer shell of the round cell opposite each other with a constant pressure setup, which we verified by a force measurement using the sensor Flexiforce A201 manufactured by Tekscan. The setup was identical for both cells. The measurement signal was bandpass filtered using the same procedure as in Wasylowski et al.[71] to extract the 1 MHz signal component. The measurement results are shown in Figure S8B. To better compare the results, the absolute value of the Hilbert-transform is depicted, representing the envelope of the ultrasound signals. It is immediately visible that the wave's amplitude through the pristine cell is about 2.57 times larger than that through the cell with the triggered CID. One explanation for this effect may be the presence of gas in the cell.[71,72] Since gas reflects ultrasonic waves almost entirely, the portions of the beam diameter covered by gas will not arrive at the receiver piezoceramic. This suggests that a considerable portion of the cell is filled with gas but not the entire signal path. The CT images in the section XRM support this assumption. In conclusion, it has been demonstrated that the applicability of ultrasound methods can also be applied to SIBs and that qualitative investigation regarding the structural state is also possible.

DISCUSSION

We tested a large variety of methods used for LIBs regarding their applicability for commercial SIBs. These batteries promise lower costs compared with their lithium-ion counterparts. Indeed, the cathode material of the investigated battery consists of a high share of iron and manganese, known as low-cost materials. Surprisingly the anode current collector is made of copper. As sodium does not form an alloy with aluminum, cheaper aluminum current collectors could be used, as investigated in Rudola et al.[73] This would enable further cost reductions.

Using centrifugal electrolyte extraction we were able to extract and analyze the electrolyte. To the best of our knowledge, no analysis of commercially used electrolyte of sodium ion batters has been published at the time of writing. The electrolyte composition is a mixture of linear and cyclic carbonates (DMC, EMC, PC, and EC), which is similar to the electrolyte used in LIBs. GC-MS shows that the electrolyte also contains

EP, which has been reported as a potential additive or co-solvent, mainly for improving low-temperature performance for LIBs.[19,20,74,75] However, to the best of our knowledge it has not been used in commercial LIBs. Coin cells assembled using the extracted electrolyte did not work as expected but showed high fluctuations in voltage. Nambu et al.[19] report that EP is unstable in the presence of lithium metal. If a similar reaction would also occur on sodium metal surfaces this could provide an explanation. Further research is necessary to clarify the reason why the extracted electrolyte did not work in half-cells. Based on the half-cell data gathered with EC:PC-based electrolyte we applied the algorithm reported in Li et al.[22] to fit the half-cell data to a full cell. Coin cells with EC:PC (1:1) with $NaPF_6$, which was reported as "the best electrolyte" in Liu et al.[15] yielded usable data, despite large overvoltages. According to Ponrouch et al.[17] adding linear carbonates such as DMC can improve the conductivity of the electrolyte, hence decreasing overvoltages. The half-cell qOCV curves were fitted to full cell data to obtain the balancing of the fresh cell. The fitting results show rather different balancing parameters for charge and discharge. Furthermore, when fitting charging data, the results indicate a small negative loss of cycleable sodium, which would indicate pre-sodification or the use of sacrificial salts as reported by Zhang et al.[76] and Jo et al.[77] Due to the discrepancies of the fitting results we can neither confirm nor dismiss the use of any pre-sodification technique for this cell. Further refinement of the half-cell measurement and subsequent fitting procedures are necessary to confidently estimate the balancing.

Hg-porosimetry, ICP-OES, SEM, EDX, and XRD were applied to characterize the active material. The particle size calculated based on porosimetry results shows good agreement with SEM observations. In contrast to intercalated lithium, intercalated sodium can be detected with EDX. Thus, the stoichiometric ratio of transition metals and sodium in the cathode active material can be analyzed using this technique. This complements established methods such as ICP-OES. We found only small differences between the ratios when comparing the ICP-OES results of an unrinsed sample with the cross-section EDX image. Both methods also revealed minor shares of calcium. Ca has been reported as a dopant to increase the performance of layered oxide cathodes in sodium ion batteries.[78] XRD was used to investigate the structure and composition of cathode active material. Even though two reflexes could not be assigned, the main phase of the cathode material was identified. The Rietveld refinement is in good agreement with the results of our EDX and ICP-OES measurements.

Electrical testing confirmed an outstanding C-rate capability. At 5C, ≈ 92% of the C/20 capacity could be extracted. The voltage-SOC relation is almost linear, facilitating SOC estimation. However, a small hysteresis is observed at lower SOCs. EIS measurements yield similar impedance spectra compared with LIBs. At low SoC, the impedance increases. Initial quality control measurements of voltage and multisine-EIS reveal a lower voltage and higher impedance for some cells. Float current measurements confirm an increased self-discharge current of these cells.

Cyclic aging of the batteries under high rates of up to 5C charge and 8C discharge leads to minor capacity fade. However, a pressure increase inside the cells triggered the CID, causing the test to stop abruptly. Ultrasonic measurements indicate substantial gassing in the affected cells. During cycling, cells exhibit fairly high temperatures, which might accelerate side reactions. The float current measurement revealed a non-reversible increase in float current after storing the cells at 55°C, which is in the same order of magnitude as the maximum surface temperature of the cells during cycling. Cells cycled with 3C8C and 5C8C behave very similar in terms of the capacity. Thus, we can reject a strong influence of the charging current on capacity fade. We attribute the earlier triggering of the CID in the case of the 5C8C cells to an increased temperature of the cell. Further research is necessary to investigate whether high temperatures are indeed as detrimental to the lifetime of this sodium-ion cell as suggested by our data.

In this paper, we present an extensive multi-method characterization of a commercial 1.2 Ah 18650 SIB cell for the first time. We investigated the electrolyte composition, identified the composition and structure of the cathode active material, and successfully applied float current measurements to obtain valuable information on the thermal stability of this sodium-ion battery. Our ultrasonic measurements complement the float current results by confirming gassing as a major issue during cyclic aging. These results can support further research and development on the application of SIBs.

In addition, we outline the transferability of a wide variety of characterization methods used for LIBs to commercial SIBs. Imaging methods, such as SEM and XRM, can be applied to SIBs without challenges. Analytical methods such as Mercury porosimetry, ICP-OES, EDX, and XRD can also be applied to SIBs. The Mercury porosimetry successfully provides insights on the pore sizes of the anode and cathode as well as on the particle diameters. This is in agreement with the SEM cross-sections. ICP-OES and EDX measurements are in agreement with the XRD experiment and confirmed an occupancy of the Mn/Fe/Ni with a 1:1:1 ratio within the cathode's layered structure of alternating metal and oxygen layers. This high share of Fe and Mn enables a low-cost SIB as the price of the cell indicates (cf. Table 1). While the aforementioned analytical methods show a good transferability to commercial SIBs, fitting of cell balancing poses a challenge due to the shape of the OCV curve of the hard carbon anode and high overpotentials related to the electrolyte as presented in the discussion. Despite the challenges in the fitting process of the cell balancing, its principal can be applied to fit the full cell qOCV. The qOCV of the commercial SIB cell investigated in this work exhibits a steep OCV (SoC) curve, providing favorable conditions for the transfer of diagnostic algorithms from established LIB cells to this SIB cell. However, the presence of a hysteresis in the lower SoC range will present a challenge for estimating the remaining energy as outlined in Quade et al.[54]

Furthermore, certain concerns pointing toward potential limitations in lifespan under high-temperature conditions were also identified: storage at temperatures above 50°C caused a persistent increase in float current, and cells at high C-rates with substantial heating suffered from an increase of internal pressure causing the CID to interrupt the electrical connection. By utilizing the testing methods of XRD and ultrasonic measurements, we can confidently state that the premature defect of these cells was triggered by excessive gas generation. However, the precise mechanisms underlying these gassing reactions necessitate additional research and focused investigation with special regard to the electrolyte and its electrochemical stability at elevated temperature. Nonetheless, the detrimental effect of substantially higher charging currents (up to 5C) on the capacity retention before the sudden cell failure by pressure-induced CID activation has to be highlighted. This underlines the high-power capabilities of this cell, showing that this early commercial SIB cell effectively bridges a gap that other cell types, as stated by ENPOLITE,[9] are unable to fill. Overcoming the challenges of thermal-induced electrolyte decomposition, this SIB cell is an ideal solution for high-power applications.

Our research shows that SIBs are not only a drop in replacement in terms of production facilities as already reported in the literature,[7] but can also benefit from the established know-how regarding multiple methods for cell characterization. As SIB cells are still considered a relatively new technology, further advancements in performance characteristics can be anticipated. The findings of this publication demonstrate that such progress is not impeded thanks to the high degree of transferability observed in most characterization methods. This suggests that ongoing research and development efforts have the potential to unlock even more significant improvements in SIB cell performance and fast deployment of SIBs on the European and world-wide markets.

In conclusion, revealing the electrolyte composition and identifying anode and cathode active material structure and composition confirms a reasonable transferability of various characterization methods to SIBs. In addition we present valuable information on thermal stability obtained by float current measurements, and identify gassing as a major issue during cyclic aging. Thereby, we provide insights into the state-of-the-art of a commercially available SIB and provide valuable information for system design and further optimization.

EXPERIMENTAL PROCEDURES

Resource availability

Lead contact

Further information and requests for resources and reagents should be directed to and will be fulfilled by the lead contact, Sebastian Klick (batteries@isea.rwth-aachen.de, https://www.carl.rwth-aachen.de).

Materials availability

This study did not generate new unique reagents.

Data and code availability

All data are available in the main text and supplemental information. Raw data of the figures shown in the main text can be accessed from RWTH Aachen University with the DOI 10.18154/RWTH-2024-04088. All other data are available from the lead contact upon reasonable request.

SUPPLEMENTAL INFORMATION

Supplemental information can be found online at https://doi.org/10.1016/j.xcrp.2024.101945.

ACKNOWLEDGMENTS

This research received funding from the Federal Ministry of Education and Research. Funding code: 03XP0302C (greenBattNutzung). Special thanks to Kevin Kistermann and Fabian Mariano from the Central Facility for Electron Microscopy (GFE) for conducting SEM investigation of prepared electrode cross-sections and sample preparation for X-ray nanotomography. Special thanks to Tobias Röhmel from Chair for Electrochemical Energy Conversion and Storage Systems, Institute for Power Electronics and Electrical Drives (ISEA) for conducting the ultrasonic measurements. Many thanks to Safion GmbH for conducting the EIS quality assurance measurements.

AUTHOR CONTRIBUTIONS

H.L., S.K., H.D., K.L.Q., A.M., A.B., M. Schütte, D.W., and M. Sonnet contributed equally to this work. Conceptualization, H.L. and S.K.; methodology, H.L., H.D., K.L.Q., A.M., A.B., M. Schütte, D.W., M. Sonnet, L.H., and A.S.; validation, S.K., G.S., F.R., and

D.U.S.; investigation, H.L., H.D., K.L.Q., A.M., A.B., M. Schütte, D.W., M. Sonnet, L.H., and A.S.; resources, G.S., F.R., J.M., and D.U.S.; data curation, H.L., H.D., K.L.Q., A.M., A.B., M. Schütte, D.W., M. Sonnet, and L.H.; writing – original draft, H.L., S.K., H.D., K.L.Q., A.M., A.B., M. Schütte, D.W., M. Sonnet, L.H., and A.S.; writing – review & editing, H.L., S.K., G.S., and F.R.; visualization, H.L., S.K., H.D., K.L.Q., A.M., A.B., M. Schütte, D.W., M. Sonnet, and L.H.; supervision, S.K., G.S., F.R., J.M., and D.U.S.; project administration, H.L., G.S., and F.R.; funding acquisition, F.R., J.M., and D.U.S.

DECLARATION OF INTERESTS

The authors declare no competing interests.

Received: August 10, 2023
Revised: February 20, 2024
Accepted: April 12, 2024
Published: May 6, 2024

REFERENCES

1. Olivetti, E.A., Ceder, G., Gaustad, G.G., and Fu, X. (2017). Lithium-Ion Battery Supply Chain Considerations: Analysis of Potential Bottlenecks in Critical Metals. Joule *1*, 229–243. https://doi.org/10.1016/j.joule.2017.08.019. https://linkinghub.elsevier.com/retrieve/pii/S2542435117300442.
2. Rudola, A., Rennie, A.J.R., Heap, R., Meysami, S.S., Lowbridge, A., Mazzali, F., Sayers, R., Wright, C.J., and Barker, J. (2021). Commercialisation of high energy density sodium-ion batteries: Faradion's journey and outlook. J. Mater. Chem. A Mater. *9*, 8279–8302. https://pubs.rsc.org/en/content/articlelanding/2021/ta/d1ta00376c.10.1039/D1TA00376C;publisher:TheRoyalSocietyofChemistry.
3. (2024). Blue Pack™ Industrial Power Battery. https://natron.energy/wp-content/uploads/natron_collateral_BluePack_Industrial_Power_Battery_021723.pdf.
4. (2023). AMTE Power gets first UN testing for sodium cell – AMTE Power. https://amtepower.com/amte-power-gets-first-un-testing-for-sodium-cell/.
5. Zhang/CnEVPost, P. (2023). CATL, BYD's sodium-ion batteries both to be in mass production within this year, report says. https://cnevpost.com/2023/04/20/catl-byd-sodium-ion-batteries-mass-production-this-year-report/.
6. redactoramexico (2023). Hina Battery Becomes 1st Battery Maker to Put Sodium-ion Batteries in Evs in China. https://batteriesnews.com/hina-battery-becomes-1st-battery-maker-put-sodium-ion-batteries-evs-china/.
7. Tapia-Ruiz, N., Armstrong, A.R., Alptekin, H., Amores, M.A., Au, H., Barker, J., Boston, R., Brant, W.R., Brittain, J.M., Chen, Y., et al. (2021). roadmap for sodium-ion batteries. JPhys Energy*3* (IOP Publishing), pp. 031503. https://doi.org/10.1088/2515-7655/ac01ef.
8. Xie, M., Wu, F., and Huang, Y. (2022). Sodium-Ion Batteries: Advanced Technology and Applications (De Gruyter). Sodium-Ion Batteries. https://doi.org/10.1515/9783110749069.
9. Dechent, P., Epp, A., Jöst, D., Preger, Y., Attia, P.M., Li, W., and Sauer, D.U. (2021). ENPOLITE: Comparing Lithium-Ion Cells across Energy, Power, Lifetime, and Temperature. ACS Energy Lett. *6*, 2351–2355. https://doi.org/10.1021/acsenergylett.1c00743.
10. Schmalstieg, J., and Sauer, D.U. (2018). Full Cell Parameterization of a High-Power Lithium-Ion Battery for a Physico-Chemical Model: Part II. Thermal Parameters and Validation. J. Electrochem. Soc. *165*, A3811–A3819. https://doi.org/10.1149/2.0331816jes. https://iopscience.iop.org/article/10.1149/2.0331816jes.
11. Ecker, M., Käbitz, S., Laresgoiti, I., and Sauer, D.U. (2015). Parameterization of a Physico-Chemical Model of a Lithium-Ion Battery: II. Model Validation. J. Electrochem. Soc. *162*, A1849–A1857. https://doi.org/10.1149/2.0541509jes; publisher: IOP Publishing. https://iopscience.iop.org/article/10.1149/2.0541509jes/meta.
12. Grützke, M., Kraft, V., Weber, W., Wendt, C., Friesen, A., Klamor, S., Winter, M., and Nowak, S. (2014). Supercritical carbon dioxide extraction of lithium-ion battery electrolytes. J. Supercrit. Fluids *94*, 216–222. https://doi.org/10.1016/j.supflu.2014.07.014. https://www.sciencedirect.com/science/article/pii/S0896844614001934.
13. Horsthemke, F., Winkler, V., Diehl, M., Winter, M., and Nowak, S. (2020). Concept for the Analysis of the Electrolyte Composition within the Cell Manufacturing Process: From Sealing to Sample Preparation. Energ. Tech. *8*, 1801081. https://doi.org/10.1002/ente.201801081.
14. Weber, F.M., Figgemeier, E., and Eichel, R.A. (2023). Stability of Lithium Electrolyte Interphase Enabling Rechargeable Lithium-Metal Batteries (RWTH Aachen University).
15. Liu, Q., Xu, R., Mu, D., Tan, G., Gao, H., Li, N., Chen, R., and Wu, F. (2022). Progress in electrolyte and interface of hard carbon and graphite anode for sodium-ion battery. Carbon Energy *4*, 458–479. https://doi.org/10.1002/cey2.120.
16. Monti, D., Jónsson, E., Boschin, A., Palacín, M.R., Ponrouch, A., and Johansson, P. (2020). Towards standard electrolytes for sodium-ion batteries: physical properties, ion solvation and ion-pairing in alkyl carbonate solvents. Phys. Chem. Chem. Phys. *22*, 22768–22777. http://xlink.rsc.org/?DOI=D0CP03639K.10.1039/D0CP03639K.
17. Ponrouch, A., Dedryvère, R., Monti, D., Demet, A.E., Ateba Mba, J.M., Croguennec, L., Masquelier, C., Johansson, P., and Palacín, M.R. (2013). Towards high energy density sodium ion batteries through electrolyte optimization. Energy Environ. Sci. *6*, 2361–2369. https://pubs.rsc.org/en/content/articlelanding/2013/ee/c3ee41379a.10.1039/C3EE41379A;publisher:TheRoyalSocietyofChemistry.
18. Tian, Z., Zou, Y., Liu, G., Wang, Y., Yin, J., Ming, J., and Alshareef, H.N. (2022). Electrolyte Solvation Structure Design for Sodium Ion Batteries. Adv. Sci. *9*, 2201207. https://doi.org/10.1002/advs.202201207.
19. Nambu, N., Ohtsuki, K., Mutsuga, H., Suzuki, Y., Takehara, M., Ue, M., and Sasaki, Y. (2012). Use of Monofluorinated Ethyl Propionates as Solvents for Lithium Secondary Batteries. Electrochemistry *80*, 746–748. https://doi.org/10.5796/electrochemistry.80.746. https://www.jstage.jst.go.jp/article/electrochemistry/80/10/80_12-4-E50726/_article.
20. Kufian, M.Z., and Majid, S.R. (2010). Performance of lithium-ion cells using 1 M LiPF6 in EC/DEC (v/v = 1/2) electrolyte with ethyl propionate additive. Ionics *16*, 409–416. https://doi.org/10.1007/s11581-009-0413-6.
21. Kasnatscheew, J., Placke, T., Streipert, B., Rothermel, S., Wagner, R., Meister, P., Laskovic, I.C., and Winter, M. (2017). A Tutorial into Practical Capacity and Mass Balancing of Lithium Ion Batteries. J. Electrochem. Soc. *164*, A2479–A2486. IOP Publishing. https://doi.org/10.1149/2.0961712jes; publisher. https://iopscience.iop.org/article/10.1149/2.0961712jes/meta.
22. Li, W., Demir, I., Cao, D., Jöst, D., Ringbeck, F., Junker, M., and Sauer, D.U. (2022). Data-driven systematic parameter identification of an electrochemical model for lithium-ion batteries with artificial intelligence. Energy Storage Mater. *44*, 557–570. https://doi.org/10.1016/j.ensm.2021.10.023. https://www.sciencedirect.com/science/article/pii/S2405829721004864.
23. Junker, M., Zhang, J., and Sauer, D.U. (2022). Prediction of Loss of Lithium Caused by Anode

Overhang Effects - Model Validation and Parameter Study. https://doi.org/10.13140/RG.2.2.34154.18884.

24. Escher, I., A. Ferrero, G., Goktas, M., and Adelhelm, P. (2022). In Situ (Operando) Electrochemical Dilatometry as a Method to Distinguish Charge Storage Mechanisms and Metal Plating Processes for Sodium and Lithium Ions in Hard Carbon Battery Electrodes. Adv. Mater. Interfac. *9*, 2100596. https://doi.org/10.1002/admi.202100596.

25. Bommier, C., Leonard, D., Jian, Z., Stickle, W.F., Greaney, P.A., and Ji, X. (2016). New Paradigms on the Nature of Solid Electrolyte Interphase Formation and Capacity Fading of Hard Carbon Anodes in Na-Ion Batteries. Adv. Mater. Interfac. *3*, 1600449. https://doi.org/10.1002/admi.201600449.

26. Li, W., Chen, J., Quade, K., Luder, D., Gong, J., and Sauer, D.U. (2022). Battery degradation diagnosis with field data, impedance-based modeling and artificial intelligence. Energy Storage Mater. *53*, 391–403. https://doi.org/10.1016/j.ensm.2022.08.021. https://www.sciencedirect.com/science/article/pii/S2405829722004500.

27. Hess, M. (2013). Kinetics and Stage Transitions of Graphite for Lithium-Ion Batteries (ETH Zurich). https://www.research-collection.ethz.ch/handle/20.500.11850/74041.10.3929/ethz-a-010000442;accepted:2017-08-17T07:37:02Z.

28. Paarmann, S., Schuld, K., and Wetzel, T. (2022). Inhomogeneous Aging in Lithium-Ion Batteries Caused by Temperature Effects. Energ. Tech. *10*, 2200384. https://doi.org/10.1002/ente.202200384.

29. Bai, Y., Liu, Y., Li, Y., Ling, L., Wu, F., and Wu, C. (2017). Mille-feuille shaped hard carbons derived from polyvinylpyrrolidone: Via environmentally friendly electrostatic spinning for sodium ion battery anodes. RSC Adv. *7*, 5519–5527. https://doi.org/10.1039/C6RA27212F.

30. Yang, B., Wang, J., Zhu, Y., Ji, K., Wang, C., Ruan, D., and Xia, Y. (2021). Engineering hard carbon with high initial coulomb efficiency for practical sodium-ion batteries. J. Power Sources *492*, 229656. https://doi.org/10.1016/j.jpowsour.2021.229656. https://www.sciencedirect.com/science/article/pii/S0378775321002007.

31. Waldmann, T., Ghanbari, N., Kasper, M., and Wohlfahrt-Mehrens, M. (2015). Correlations between Electrochemical Data and Results from Post-Mortem Analysis of Aged Lithium-Ion Batteries. J. Electrochem. Soc. *162*, A1500–A1505. https://doi.org/10.1149/2.0411508jes; publisher: IOP Publishing. https://iopscience.iop.org/article/10.1149/2.0411508jes/meta.

32. Fuchs, G., Willenberg, L., Ringbeck, F., and Sauer, D.U. (2019). Post-Mortem Analysis of Inhomogeneous Induced Pressure on Commercial Lithium-Ion Pouch Cells and Their Effects. Sustainability *11*, 6738. Multidisciplinary Digital Publishing Institute. https://doi.org/10.3390/su11236738. https://www.mdpi.com/2071-1050/11/23/6738.

33. Takahashi, K., and Srinivasan, V. (2015). Examination of Graphite Particle Cracking as a Failure Mode in Lithium-Ion Batteries: A Model-Experimental Study. J. Electrochem. Soc. *162*, A635–A645. IOP Publishing. https://doi.org/10.1149/2.0281504jes; publisher. https://iopscience.iop.org/article/10.1149/2.0281504jes/meta.

34. Kuntz, P., Raccurt, O., Azaïs, P., Richter, K., Waldmann, T., Wohlfahrt-Mehrens, M., Bardet, M., Buzlukov, A., and Genies, S. (2021). Identification of Degradation Mechanisms by Post-Mortem Analysis for High Power and High Energy Commercial Li-Ion Cells after Electric Vehicle Aging. Batteries *7*, 48. Multidisciplinary Digital Publishing Institute. https://doi.org/10.3390/batteries7030048; number: 3 Publisher. https://www.mdpi.com/2313-0105/7/3/48.

35. Waldmann, T., Wilka, M., Kasper, M., Fleischhammer, M., and Wohlfahrt-Mehrens, M. (2014). Temperature dependent ageing mechanisms in Lithium-ion batteries – A Post-Mortem study. J. Power Sources *262*, 129–135. https://doi.org/10.1016/j.jpowsour.2014.03.112. https://www.sciencedirect.com/science/article/pii/S0378775314004352.

36. Thompson, A. (2001). X-Ray Data Booklet (Lawrence Berkeley National Laboratory, University of California).

37. Jankowski, P., Lindahl, N., Weidow, J., Wieczorek, W., and Johansson, P. (2018). Impact of Sulfur-Containing Additives on Lithium-Ion Battery Performance: From Computational Predictions to Full-Cell Assessments. ACS Appl. Energy Mater. *1*, 2582–2591. https://doi.org/10.1021/acsaem.8b00295.

38. Tong, B., Song, Z., Wan, H., Feng, W., Armand, M., Liu, J., Zhang, H., and Zhou, Z. (2021). Sulfur-containing compounds as electrolyte additives for lithium-ion batteries. InfoMat *3*, 1364–1392. https://doi.org/10.1002/inf2.12235.

39. Wu, Z., Li, S., Zheng, Y., Zhang, Z., Umesh, E., Zheng, B., Zheng, X., and Yang, Y. (2018). The Roles of Sulfur-Containing Additives and Their Working Mechanism on the Temperature-Dependent Performances of Li-Ion Batteries. J. Electrochem. Soc. *165*, A2792–A2800. https://doi.org/10.1149/2.0331811jes. https://iopscience.iop.org/article/10.1149/2.0331811jes.

40. Singh, V.K., Singh, S.K., Gupta, H., Shalu, Balo, L., Tripathi, A.K., Verma, Y.L., and Singh, R.K. (2018). Electrochemical investigations of Na0.7CoO2 cathode with PEO-NaTFSI-BMIMTFSI electrolyte as promising material for Na-rechargeable battery. J. Solid State Electrochem. *22*, 1909–1919. https://doi.org/10.1007/s10008-018-3891-5.

41. Fondard, J., Irisarri, E., Courrèges, C., Palacin, M.R., Ponrouch, A., and Dedryvère, R. (2020). SEI Composition on Hard Carbon in Na-Ion Batteries After Long Cycling: Influence of Salts (NaPF 6, NaTFSI) and Additives (FEC, DMCF). J. Electrochem. Soc. *167*, 070526. https://iopscience.iop.org/article/10.1149/1945-7111/ab75fd.

42. Harris, K.D.M., Tremayne, M., and Kariuki, B.M. (2001). Contemporary Advances in the Use of Powder X-Ray Diffraction for Structure Determination. Angew. Chem., Int. Ed. Engl. *40*, 1626–1651. https://doi.org/10.1002/1521-3773(20010504)40:9<1626::AID-ANIE16260>3.0.CO;2-7.

43. WinXPow (2005). https://www.stoe.com/products/winxpow/.

44. Rodríguez-Carvajal, J. (1993). Recent advances in magnetic structure determination by neutron powder diffraction. Phys. B Condens. Matter *192*, 55–69. https://doi.org/10.1016/0921-4526(93)90108-I. https://www.sciencedirect.com/science/article/pii/092145269390108I.

45. Mao, Q., Zhang, C., Yang, W., Yang, J., Sun, L., Hao, Y., and Liu, X. (2019). Mitigating the voltage fading and lattice cell variations of O3-NaNi0.2Fe0.35Mn0.45O2 for high performance Na-ion battery cathode by Zn doping. J. Alloys Compd. *794*, 509–517. https://doi.org/10.1016/j.jallcom.2019.04.271. https://www.sciencedirect.com/science/article/pii/S0925838819315713.

46. Lamb, J., Stokes, L., and Manthiram, A. (2020). Delineating the Capacity Fading Mechanisms of Na(Ni0.3Fe0.4Mn0.3)O2 at Higher Operating Voltages in Sodium-Ion Cells. Chem. Mater. *32*, 7389–7396. https://doi.org/10.1021/acs.chemmater.0c02292.

47. Van Bommel, A., and Dahn, J. (2008). Synthesis of Dense and Spherical Hydroxide Particles as Precursors to NMC Oxides for Positive Electrode Materials in Lithium-ion Batteries. Meet. Abstr. 1137. IOP Publishing. https://doi.org/10.1149/MA2008-02/12/1137; publisher. https://iopscience.iop.org/article/10.1149/MA2008-02/12/1137/meta.

48. Waag, W., Käbitz, S., and Sauer, D.U. (2013). Experimental investigation of the lithium-ion battery impedance characteristic at various conditions and aging states and its influence on the application. Appl. Energy *102*, 885–897. https://doi.org/10.1016/j.apenergy.2012.09.030. https://www.sciencedirect.com/science/article/pii/S030626191200671X.

49. Kim, J., Park, S., Hwang, S., and Yoon, W.S. (2022). Principles and Applications of Galvanostatic Intermittent Titration Technique for Lithium-ion Batteries. J. Electrochem. Sci. Technol. *13*, 19–31. The Korean Electrochemical Society. https://doi.org/10.33961/jecst.2021.00836.

50. Marongiu, A., Nußbaum, F.G.W., Waag, W., Garmendia, M., and Sauer, D.U. (2016). Comprehensive study of the influence of aging on the hysteresis behavior of a lithium iron phosphate cathode-based lithium ion battery – An experimental investigation of the hysteresis. Appl. Energy *171*, 629–645. https://doi.org/10.1016/j.apenergy.2016.02.086. https://www.sciencedirect.com/science/article/pii/S030626191630232X.

51. Lewerenz, M., Marongiu, A., Warnecke, A., and Sauer, D.U. (2017). Differential voltage analysis as a tool for analyzing inhomogeneous aging: A case study for LiFePO4|Graphite cylindrical cells. J. Power Sources *368*, 57–67. https://www.sciencedirect.com/science/article/pii/S0378775317312788.10.1016/j.jpowsour.2017.09.059.

52. Nemeth, T., Schröer, P., Kuipers, M., and Sauer, D.U. (2020). Lithium titanate oxide battery cells for high-power automotive applications – Electro-thermal properties, aging behavior and cost considerations. J. Energy Storage *31*, 101656. https://doi.org/10.1016/j.est.2020.101656. https://www.sciencedirect.com/science/article/pii/S2352152X20314936.

53. Bank, T., Klamor, S., Löffler, N., and Sauer, D.U. (2021). Performance benchmark of state-of-the-art high-power lithium-ion cells and implications for their usability in low-voltage applications. J. Energy Storage *36*, 102383. https://doi.org/10.1016/j.est.2021.102383. https://www.sciencedirect.com/science/article/pii/S2352152X21001389.

54. Quade, K.L., Jöst, D., Sauer, D.U., and Li, W. (2023). Understanding the Energy Potential of Lithium-Ion Batteries: Definition and Estimation of the State of Energy. Batteries & Supercaps *6*. n/a(n/a):e202300152.. https://doi.org/10.1002/batt.202300152

55. Blömeke, A., Quade, K.L., Jöst, D., Li, W., Ringbeck, F., and Sauer, D.U. (2022). Properties of a Lithium-Ion Battery as a Partner of Power Electronics. In 2022 24th European Conference on Power Electronics and Applications (EPE'22 ECCE Europe), pp. 1–10.

56. Shafiei Sabet, P., Sauer, D.U., and Ivers-Tiffée, E. (2019). Analysis of Predominant Processes in Electrochemical Impedance Spectra and Investigation of Aging Processes of Lithium-Ion Batteries with Layered Oxide Cathodes and Graphitic Anodes. Medium: online Series Number: 138 Series: Aachener Beiträge des ISEA.

57. Theiler, M., Endisch, C., and Lewerenz, M. (2021). Float Current Analysis for Fast Calendar Aging Assessment of 18650 Li(NiCoAl)O2/Graphite Cells. Batteries *7*, 22. Multidisciplinary Digital Publishing Institute. https://doi.org/10.3390/batteries7020022. https://www.mdpi.com/2313-0105/7/2/22.

58. Broussely, M., Herreyre, S., Biensan, P., Kasztejna, P., Nechev, K., and Staniewicz, R.J. (2001). Aging mechanism in Li ion cells and calendar life predictions. J. Power Sources *97–98*, 13–21. https://doi.org/10.1016/S0378-7753(01)00722-4. https://www.sciencedirect.com/science/article/pii/S0378775301007224.

59. Chahbaz, A., Meishner, F., Li, W., Ünlübayir, C., and Uwe Sauer, D. (2021). Non-invasive identification of calendar and cyclic ageing mechanisms for lithium-titanate-oxide batteries. Energy Storage Mater. *42*, 794–805. https://doi.org/10.1016/j.ensm.2021.08.025. https://www.sciencedirect.com/science/article/pii/S2405829721003950.

60. Spingler, F.B., Naumann, M., and Jossen, A. (2020). Capacity Recovery Effect in Commercial LiFePO4/Graphite Cells. J. Electrochem. Soc. *167*, 040526. IOP Publishing. https://doi.org/10.1149/1945-7111/ab7900.

61. Harlow, J.E., Ma, X., Li, J., Logan, E., Liu, Y., Zhang, N., Ma, L., Glazier, S.L., Cormier, M.M.E., Genovese, M., et al. (2019). A Wide Range of Testing Results on an Excellent Lithium-Ion Cell Chemistry to be used as Benchmarks for New Battery Technologies. J. Electrochem. Soc. *166*, A3031–A3044. https://doi.org/10.1149/2.0981913jes; publisher: IOP Publishing. https://iopscience.iop.org/article/10.1149/2.0981913jes/meta.

62. Li, J., Li, H., Stone, W., Glazier, S., and Dahn, J.R. (2018). Development of Electrolytes for Single Crystal NMC532/Artificial Graphite Cells with Long Lifetime. J. Electrochem. Soc. *165*, A626–A635. https://doi.org/10.1149/2.0971803jes; publisher: IOP Publishing. https://iopscience.iop.org/article/10.1149/2.0971803jes/meta.

63. Pietsch, P., and Wood, V. (2017). X-Ray Tomography for Lithium Ion Battery Research: A Practical Guide. Annu. Rev. Mater. Res. *47*, 451–479. https://doi.org/10.1146/annurev-matsci-070616-123957.

64. Feldkamp, L.A., Davis, L.C., and Kress, J.W. (1984). Practical cone-beam algorithm. J. Opt. Soc. Am. *6* (1). https://opg.optica.org/josaa/fulltext.cfm?uri=josaa-1-6-612&id=996.

65. Pfrang, A., Kersys, A., Kriston, A., Sauer, D.U., Rahe, C., Käbitz, S., and Figgemeier, E. (2019). Geometrical Inhomogeneities as Cause of Mechanical Failure in Commercial 18650 Lithium Ion Cells. J. Electrochem. Soc. *166*, A3745–A3752. IOP Publishing. https://doi.org/10.1149/2.0551914jes; publisher. https://iopscience.iop.org/article/10.1149/2.0551914jes/meta.

66. Rahe, C., Kelly, S.T., Rad, M.N., Sauer, D.U., Mayer, J., and Figgemeier, E. (2019). Nanoscale X-ray imaging of ageing in automotive lithium ion battery cells. J. Power Sources *433*, 126631. https://doi.org/10.1016/j.jpowsour.2019.05.039. https://www.sciencedirect.com/science/article/pii/S0378775319305944.

67. Frisco, S., Kumar, A., Whitacre, J.F., and Litster, S. (2016). Understanding Li-Ion Battery Anode Degradation and Pore Morphological Changes through Nano-Resolution X-ray Computed Tomography. J. Electrochem. Soc. *163*, A2636–A2640. https://doi.org/10.1149/2.0681613jes; publisher: IOP Publishing. https://iopscience.iop.org/article/10.1149/2.0681613jes/meta.

68. Hsieh, A.G., Steingart, D.A., Bhadra, S., Hertzberg, B.J., Gjeltema, P.J., Goy, A., and Fleischer, J.W. (2015). Electrochemical-acoustic time of flight: in operando correlation of physical dynamics with battery charge and health. Energy Environ. Sci. *8*, 1569–1577. Royal Society of Chemistry. https://doi.org/10.1039/C5EE00111K. https://pubs.rsc.org/en/content/articlelanding/2015/ee/c5ee00111k.

69. Deng, Z., Huang, Z., Shen, Y., Huang, Y., Ding, H., Luscombe, A., Johnson, M., Harlow, J.E., Gauthier, R., and Dahn, J.R. (2020). Ultrasonic Scanning to Observe Wetting and "Unwetting" in Li-Ion Pouch Cells. Joule *4*, 2017–2029. https://doi.org/10.1016/j.joule.2020.07.014. https://www.sciencedirect.com/science/article/pii/S2542435120303329.

70. Zhang, Y.S., Pallipurath Radhakrishnan, A.N., Robinson, J.B., Owen, R.E., Tranter, T.G., Kendrick, E., Shearing, P.R., and Brett, D.J.L. (2021). In Situ Ultrasound Acoustic Measurement of the Lithium-Ion Battery Electrode Drying Process. ACS Appl. Mater. Interfaces *13*, 36605–36620. American Chemical Society. https://doi.org/10.1021/acsami.1c10472.

71. Wasylowski, D., Kisseler, N., Ditler, H., Sonnet, M., Fuchs, G., Ringbeck, F., and Sauer, D.U. (2022). Spatially resolving lithium-ion battery aging by open-hardware scanning acoustic imaging. J. Power Sources *521*, 230825. https://www.sciencedirect.com/science/article/pii/S0378775321013136.10.1016/j.jpowsour.2021.230825.

72. Wasylowski, D., Neubauer, S., Faber, M., Ditler, H., Sonnet, M., Blömeke, A., Dechent, P., Gitis, A., and Sauer, D.U. (2023). In situ tomography of lithium-ion battery cells enabled by scanning acoustic imaging. J. Power Sources *580*, 233295. https://www.sciencedirect.com/science/article/pii/S0378775323006717.10.1016/j.jpowsour.2023.233295.

73. Rudola, A., Wright, C.J., and Barker, J. (2021). Reviewing the Safe Shipping of Lithium-Ion and Sodium-Ion Cells: A Materials Chemistry Perspective. Energy Mater. Adv. *2021*, 2021–9798460. https://doi.org/10.34133/2021/9798460.

74. Azzam, M., Ehrensberger, M., Scheuer, R., Endisch, C., and Lewerenz, M. (2023). Long-Term Self-Discharge Measurements and Modelling for Various Cell Types and Cell Potentials. Energies *16*, 3889. https://doi.org/10.3390/en16093889. https://www.mdpi.com/1996-1073/16/9/3889.

75. Ohta, A., Koshina, H., Okuno, H., and Murai, H. (1995). Relationship between carbonaceous materials and electrolyte in secondary lithium-ion batteries. J. Power Sources *54*, 6–10. https://doi.org/10.1016/0378-7753(94)02031-W. https://www.sciencedirect.com/science/article/pii/037877539402031W.

76. Zhang, Z., Zhang, R., Rajagopalan, R., Tang, Z., Sun, D., Wang, H., and Tang, Y. (2022). A high-capacity self-sacrificial additive based on electroactive sodiated carbonyl groups for sodium-ion batteries. Chem. Commun. *58*, 8702–8705. https://pubs.rsc.org/en/content/articlelanding/2022/cc/d2cc01812h.10.1039/D2CC01812H;publisher: TheRoyalSocietyofChemistry.

77. Jo, C.H., Choi, J.U., Yashiro, H., and Myung, S.T. (2019). Controllable charge capacity using a black additive for high-energy-density sodium-ion batteries. J. Mater. Chem. A Mater. *7*, 3903–3909. The Royal Society of Chemistry. https://doi.org/10.1039/C8TA09833F. https://pubs.rsc.org/en/content/articlelanding/2019/ta/c8ta09833f.

78. Fu, H., Wang, Y.P., Fan, G., Guo, S., Xie, X., Cao, X., Lu, B., Long, M., Zhou, J., and Liang, S. (2022). Synergetic stability enhancement with magnesium and calcium ion substitution for ni/mn-based p2-type sodium-ion battery cathodes. Chem. Sci. *13*, 726–736. https://doi.org/10.1039/D1SC05715D.